# Generalized kinetic hierarchy for the Boltzmann equation with application to incompressible turbulence

Yiming Qi (岐亦铭),[1,*] Jie Shen (沈杰),[2] Lian-Ping Wang (王连平),[2] Tianbai Xiao (肖天白),[1,†] Zhaoli Guo (郭照立),[3] Yonghao Zhang (张勇豪),[1] and Shiyi Chen (陈十一)[4,5]

[1]*Centre for Interdisciplinary Research in Fluids, Institute of Mechanics, Chinese Academy of Sciences, Beijing 100190, China*

[2]*Guangdong Provincial Key Laboratory of Turbulence Research and Applications, Center for Complex Flows and Soft Matter Research and Department of Mechanics and Aerospace Engineering, Southern University of Science and Technology, Shenzhen, Guangdong 518055, China*

[3]*Institute of Interdisciplinary Research for Mathematics and Applied Science, Huazhong University of Science and Technology, Wuhan, Hubei 430074, China*

[4]*Eastern Institute for Advanced Study, Eastern Institute of Technology, Ningbo, Zhejiang 315200, China*

[5]*State Key Laboratory for Turbulence and Complex Systems, College of Engineering, Peking University, Beijing 100871, China*

(Received 19 February 2026; revised 21 August 2026; accepted 20 October 2026; published 6 November 2026)

A unified theoretical framework is given to rigorously describe the hierarchy of macroscopic equations recovered from the Boltzmann model equation. The framework first integrates the Chapman-Enskog (CE) analysis with the Hermite expansions of the equilibrium distribution function. The framework is then augmented by a Hilbert expansion of the Hermite coefficients with respect to the relaxation time. This additional step removes an implicit assumption in existing analyses [X. Shan *et al.*, J. Fluid Mech. **550**, 413 (2006)], namely that all Hermite coefficients share the same relaxation time order, which limits the applicability of the Boltzmann model equation for some existing kinetic models and is inconsistent with the multiscale asymptotics underlying the CE analysis. Within the present formulation, a richer kinetic hierarchy can be constructed, in which different Hilbert coefficients correspond to distinct moment equations, providing a systematic route for recovering generalized macroscopic equations. To demonstrate the applicability of our proposed framework, a general form of the kinetic model is analyzed for incompressible flows, encompassing four representative models from the literature together with an additional model derived within the present framework. The proposed model introduces an oscillation-suppression term in the Hilbert coefficients, yielding a continuity equation that combines features of artificial compressibility and penalty methods. This modification effectively suppresses spurious pressure without introducing additional auxiliary variables. Simulations of decaying turbulence confirm the theoretical findings and demonstrate the effectiveness of the proposed model.

DOI: 10.1103/g64s-xfj8

## I. INTRODUCTION

Mesoscopic computational fluid dynamics (CFD) methods are founded on the Boltzmann equation, which governs the evolution of the distribution function in the phase space and provides a unified description of gas flows across different scales. The central objective of such kinetic-theory based CFD methods is to derive macroscopic equations for hydrodynamic variables from the prescribed model Boltzmann equation. Two principal analytical approaches are commonly employed for this purpose: the Chapman-Enskog (CE) analysis [1] and Grad's Hermite-moment analysis [2,3].

The CE analysis treats the Knudsen number as a small parameter and expands the Boltzmann model equation into an asymptotic series in the Knudsen number, or equivalently, the relaxation time [4]. Since this procedure does not yield closed-form expressions, the series is typically truncated at a given order, followed by the velocity moments to obtain macroscopic equations. For the Boltzmann equation, retaining the leading-order term recovers the inviscid Euler equations, the first-order truncation yields the Navier-Stokes (NS) equations, and higher-order truncations lead to the Burnett [5] and super-Burnett equations, with differences manifested in the stress and heat flux. In fact, the CE expansion can be recast as nonlinear constitutive relations for stress and heat flux in the Maxwell-Truesdell-Green iteration [6,7].

In contrast, Grad's analysis expands the distribution function as a finite multidimensional Hermite polynomial with the Maxwellian equilibrium as the weighting function [8]. By retaining a prescribed number of Hermite coefficients, one obtains closed systems of macroscopic moment equations, such as the Grad 13- or 26-moment equations [2,3]. Despite their different constructions, both high-order CE systems (e.g., Burnett equations) and Grad moment systems commonly suffer from practical and theoretical difficulties, including complexity in computing the high-order derivatives, ambiguity in implementing the boundary conditions, and mathematical issues such as ill posedness [9,10] or lack of hyperbolicity [11].

These two approaches have profoundly shaped the subsequent developments in the Boltzmann-equation based

*Contact author: qiyiming@imech.ac.cn
†Contact author: txiao@imech.ac.cn

 ©2026 American Physical Society

mesoscopic methods [12–15]. Shan *et al.* [16] combined a Hermite expansion of the equilibrium distribution with a first-order CE analysis to reformulate the Boltzmann–Bhatnagar-Gross-Krook (BGK) equation [17] as a hierarchy of macroscopic equations for the Hermite coefficients, thereby revealing the intrinsic multiscale kinetic representation underlying Boltzmann model equations. This formulation, however, implicitly assumes that equilibrium Hermite coefficients at all orders scale identically with the Knudsen number (or relaxation time). In contrast, the CE analysis is inherently multiscale, relying on an asymptotic expansion in the relaxation time. In the present work, we therefore argue that the equilibrium coefficients themselves should exhibit distinct multiscale behavior, which motivates the introduction of a Hilbert expansion [1] for these coefficients. The resulting Boltzmann model system not only recovers the original formulation of Shan *et al.* [16] as a limiting case but also yields a richer dynamical hierarchy, thereby extending the multiscale kinetic framework.

Introducing a Hilbert series for the equilibrium Hermite coefficients is equivalent to modifying the equilibrium distribution with higher-order relaxation-time corrections. Precedents for such treatments exist in mesoscopic modeling: for example, the Shakhov model [18], proposed to remedy the fixed unity Prandtl number of the BGK model [17], and the lattice kinetic scheme, widely used for thermal [19,20], multiphase [21], and non-Newtonian flows [22,23], both incorporate relaxation-time-dependent corrections in the equilibrium. More recently, Chen *et al.* [24] introduced an inverse-design framework in which an undetermined source term is added to the BGK collision, and its velocity moment constraints and Hermite expansion are determined by matching a CE analysis to the macroscopic equations. These models are, in essence, first-order relaxation-time modifications calibrated to recover prescribed macroscopic behavior. However, such corrections are often introduced in an *ad hoc* manner, offering limited physical interpretation and devoid of a unified theoretical framework. To address this gap, the present study systematically develops a multiscale analysis of Hermite equilibria incorporating a Hilbert expansion, indicating that these correction terms must satisfy asymptotic properties with respect to the relaxation time, and constructs a generalized kinetic theory representation applicable to the Boltzmann model equations.

To demonstrate the capability of our proposed analysis, we shall focus on incompressible flow modeling, one of the most widely used applications of the Boltzmann model equations [25–28], and carry out detailed theoretical comparisons and model derivations. We consider four representative models that are commonly used in practice: the athermal model [29], the He-Luo model [30], the Guo model [31], and the Zhang model [32]. In particular, the He-Luo model can be obtained by a decomposition of the density into a mean and a fluctuation and neglecting higher-order Mach-number terms for the athermal model. Although the Guo and Zhang models recover the same macroscopic equations, they differ in the construction of the equilibrium distribution: the Zhang model employs a unified Hermite-polynomial representation for all discrete velocities, whereas the Guo model prescribes distinct equilibrium forms for different discrete velocities. We emphasize that all kinetic models considered in this work are intrinsically weakly compressible at the hydrodynamic level, rather than enforcing a strict incompressibility constraint. The incompressible behavior discussed here refers to the target macroscopic regime and is recovered only asymptotically in the low-Mach-number limit, where the governing equations reduce to the incompressible Navier-Stokes equations.

When applied to incompressible flows, these models recover macroscopic equations that effectively correspond to an artificial compressibility method [33–35]. As a result, in addition to the hydrodynamic mechanical pressure, spurious acoustic (artificial noise) pressure is introduced by the artificial compressibility. Compared with the athermal model, the He-Luo, Guo, and Zhang models alleviate this noise to varying degrees but do not eliminate it entirely. In existing macroscopic formulations and multiple-relaxation-time lattice Boltzmann methods (MRT-LBE) [36], such acoustic artifacts are commonly suppressed by introducing a bulk viscosity [37–39]. By contrast, here we develop a model (hereafter referred to as the Qi model) that completely suppresses artificial noise without invoking bulk viscosity, velocity divergence, or auxiliary variables beyond density and velocity. Our theoretical analysis shows that the recovered macroscopic equations are equivalent to a hybrid formulation combining artificial compressibility [33] with a penalty method [40], while the higher-order errors in the viscous stress do not surpass those of the He-Luo model. To systematically assess these models, we perform simulations of incompressible decaying turbulence, which involves both rapidly decaying mechanical pressure and long-term spurious acoustic pressure with distinct timescales [38,41], thereby delivering robust artificial-noise suppression and precise pressure evolution.

This study aims to establish a general kinetic hierarchy for the Boltzmann model equation and to apply this framework to systematically analyze prior kinetic models for incompressible flows, and, in addition, to develop a model. By applying these models to simulate incompressible decaying turbulence, we provide a quantitative comparison of their ability to suppress artificial noise.

The paper is organized as follows. Section II presents a generalized CE analysis combined with the Hermite expansion, in which the corresponding Hermite coefficients are expressed as Hilbert series, leading to a kinetic hierarchy analogous to that of Shan *et al.* [16]. Section III applies our proposed framework to analyze the kinetic models for incompressible flows, providing a unified representation of the athermal, He-Luo, Guo, and Zhang models, as well as the proposed Qi model, with particular emphasis on the recovered macroscopic equations and high-order errors in the viscous stress. Section IV simulates three-dimensional incompressible decaying homogeneous turbulence, analyzing turbulent statistics and instantaneous strain-rate contours to elucidate differences among these models. Section V concludes with a summary and discussion.

## II. A GENERALIZED CHAPMAN-ENSKOG ANALYSIS BASED ON HERMITE POLYNOMIALS

To introduce the proposed analysis, we consider a three-dimensional fluid system. Let $\boldsymbol{x}$ denote the spatial coordinates,

$\boldsymbol{\xi}$ the particle velocity, $t$ the time, and $\nabla$ the gradient operator. The particle distribution function $f(\boldsymbol{x}, \boldsymbol{\xi}, t)$ evolves according to a prescribed Boltzmann model equation,

$$\frac{Df}{Dt} = \frac{\partial f}{\partial t} + \boldsymbol{\xi} \cdot \nabla f + \boldsymbol{b} \cdot \nabla_{\boldsymbol{\xi}} f = -\frac{f - f^{\mathrm{eq}}}{\tau}, \tag{1}$$

where $\tau$ is the relaxation time, $\boldsymbol{b}$ represents an external body force, and $f^{\mathrm{eq}}$ is the local equilibrium distribution in the BGK collision model [17]. For the BGK model, the equilibrium is the Maxwellian, $f^{\mathrm{eq}} = \rho(2\pi RT)^{-3/2} \exp[-c^2/(2RT)]$, with density $\rho$, gas constant $R$, temperature $T$, and thermal fluctuating velocity $\boldsymbol{c} = \boldsymbol{\xi} - \boldsymbol{u}$. In addition, the equilibrium in the kinetic model must satisfy the conservation relation

$$\int (f^{\mathrm{eq}} - f)\boldsymbol{\psi} d\boldsymbol{\xi} = \boldsymbol{0}, \tag{2}$$

where $\boldsymbol{\psi}$ is the conserved variables or the athermal flows considered here, and mass and momentum are conserved, with $\boldsymbol{\psi} = [1, \boldsymbol{\xi}]^T$. The choice of $\boldsymbol{\psi}$ defines the conserved moments of the collision operator; incompressibility emerges only asymptotically in the low-Mach-number limit. In Boltzmann-equation-based numerical methods, the equilibrium distribution is commonly approximated by a finite $R$th-order Hermite expansion,

$$f^{\mathrm{eq}} \approx f^{\mathrm{eq},(R)} = w(\xi, c_s) \sum_{r=0}^{R} \frac{1}{r!} A_i^{(r)} \mathcal{H}_i^{(r)}, \; \boldsymbol{A}^{(r)} \sim \boldsymbol{O}(\tau^0), \tag{3}$$

where $w = \exp[-\xi^2/(2c_s^2)]/(2\pi c_s^2)^{3/2}$ is the weight function associated with the reference sound speed $c_s$ and $\mathcal{H}_i^{(r)}$ denotes the $r$th-order Hermite polynomial [8]. The corresponding coefficients $A_i^{(r)}$ are all of order $\boldsymbol{O}(\tau^0)$, which will be demonstrated subsequently.

Taking the relaxation time $\tau$ as a small parameter, the CE expansion is then applied through a Maxwellian iteration,

$$f = \left(1 + \tau \frac{D}{Dt}\right)^{-1} f^{\mathrm{eq}} \approx \sum_{p=0}^{P} \left(-\tau \frac{D}{Dt}\right)^p f^{\mathrm{eq}}, \tag{4}$$

where $P$ is the truncation order of the CE expansion. Unless otherwise stated, all subsequent analyses in this work are based on a $P$th-order CE expansion. When the CE expansion is combined with a $R$th-order Hermite approximation of the equilibrium, the resulting distribution function takes the form

$$f \approx f^{(R)} \approx \sum_{p=0}^{P} \sum_{r=0}^{R} \frac{1}{r!} \left(-\tau \frac{D}{Dt}\right)^p w(\xi, c_s) A_i^{(r)} \mathcal{H}_i^{(r)}, \tag{5}$$

which constitutes the kinetic hierarchy originally formulated by Shan *et al.* [16].

However, the hierarchy of Shan *et al.* [16] presumes that all equilibrium Hermite coefficients are $\boldsymbol{O}(\tau^0)$, an assumption that does not hold for several important extensions of the Boltzmann model equation. In the Shakhov model [18], for example, the collision operator may be written in BGK form with an effective equilibrium whose third-order Hermite coefficient is proportional to the heat flux and is therefore $\boldsymbol{O}(\tau)$ under CE scaling. Likewise, lattice kinetic schemes [19,22,23] introduce $\boldsymbol{O}(\tau)$ corrections to the equilibrium distribution to recover prescribed transport properties, including the Prandtl number and non-Newtonian viscosity. In the inverse-designed formulations [24], the additional source term is Hermite expanded and constrained by matching the CE expansion to the target macroscopic equations; when absorbed into the BGK equilibrium, it likewise constitutes an $\boldsymbol{O}(\tau)$ correction. These relaxation-time-dependent equilibria are therefore not encompassed by the hierarchy of Shan *et al.* [16].

We further argue that the Hermite coefficients themselves should admit a Hilbert expansion [1],

$$\boldsymbol{A}^{(r)} \approx \sum_{q=0}^{Q} \tau^q \boldsymbol{a}^{(r,q)}, \quad \boldsymbol{a}^{(r,q)} \sim \boldsymbol{O}(\tau^0), \tag{6}$$

where $\boldsymbol{a}^{(r,q)}$ denotes the Hilbert coefficient at the $q$th order in the relaxation time. This leads to a generalized equilibrium expansion $f^{\mathrm{eq},(R,Q)}$, namely,

$$f^{\mathrm{eq},(R)} \approx f^{\mathrm{eq},(R,Q)} = w(\xi, c_s) \sum_{r=0}^{R} \sum_{q=0}^{Q} \frac{\tau^q}{r!} a_i^{(r,q)} \mathcal{H}_i^{(r)}, \tag{7}$$

where the first and second superscripts in the parentheses indicate the orders of the Hermite and Hilbert expansions, respectively. For the proposed framework, the conservation relation Eq. (2) is equivalent to retaining only the zeroth-order Hilbert term, i.e.,

$$\int [f^{\mathrm{eq},(\infty,0)} - f]\boldsymbol{\psi} d\boldsymbol{\xi} = \boldsymbol{0},$$

$$f^{\mathrm{eq},(\infty,0)} = w(\xi, c_s) \sum_{r=0}^{\infty} \frac{1}{r!} a_i^{(r,0)} \mathcal{H}_i^{(r)}. \tag{8}$$

The CE expansion, Hermite polynomial, and Hilbert series can be combined to yield a generalized CE representation of the distribution function

$$f \approx f^{(R)} \approx \sum_{p=0}^{P} \sum_{r=0}^{R} \sum_{q=0}^{Q} \frac{1}{r!} \left(-\tau \frac{D}{Dt}\right)^p w(\xi, c_s) \tau^q a_i^{(r,q)} \mathcal{H}_i^{(r)}. \tag{9}$$

Although the convergence of the proposed series expansion cannot be rigorously established, it is well known that the CE expansion is, in general, asymptotic rather than convergent [10]. By analogy with the CE analysis, we therefore assume that $D/Dt$ is a bounded operator and that the distribution function $f$ is sufficiently smooth. Under these assumptions, the present expansion should be regarded as an asymptotic series, which remains valid for deriving hydrodynamic systems truncated at a finite order.

Two remarks on the interpretation of the Hilbert expansion Eq. (6) are noteworthy. First, $f^{\mathrm{eq}}$ in the Boltzmann model equation Eq. (1) is a modeling construct rather than the physical Maxwellian equilibrium of the full Boltzmann equation. Any $f^{\mathrm{eq}}$ satisfying the conservation relation Eq. (2) and recovering the target macroscopic equations through CE analysis is admissible. Thus, the Hilbert expansion provides a systematic closure: the relaxation-time dependence

of equilibrium coefficients does not modify the BGK relaxation mechanism, but introduces controlled higher-order corrections. Second, since $\tau$ is the CE expansion parameter, each correction $\tau^q \boldsymbol{a}^{(r,q)}$ enters the macroscopic equations at a prescribed asymptotic order, preserving the multiscale consistency.

To construct the corresponding kinetic hierarchy, an approximation truncated at the NS level is adopted. The detailed derivation of the resulting governing equations in this section's subsequent content is provided in Appendix A. After a systematic simplification with the properties of Hermite polynomials, the distribution $f^{(R)}$ reduces to

$$
\begin{aligned}
f^{(R)} &= \sum_{r=0}^{R} \frac{1}{r!}\left[1-\tau\frac{D}{Dt}+O(\tau^2)\right] w(\xi,c_s)\left[a_{\boldsymbol{i}}^{(r,0)}+\tau a_{\boldsymbol{i}}^{(r,1)}+O(\tau^2)\right]\mathcal{H}_{\boldsymbol{i}}^{(r)} \\
&= w\left\{\begin{array}{l}
\sum_{r=0}^{R}\frac{1}{r!}a_{i_1\cdots i_r}^{(r,0)}\mathcal{H}_{i_1\cdots i_r}^{(r)}-\tau\left(\frac{\partial a^{(0,0)}}{\partial t}+c_s\nabla_i a_i^{(1,0)}-a^{(0,1)}\right)\mathcal{H}^{(0)} \\
-\tau\sum_{r=1}^{R-1}\frac{1}{r!}\left[\begin{array}{l}\partial a_{i_1\cdots i_r}^{(r,0)}/\partial t+c_s\nabla_{i_{r+1}}a_{i_1\cdots i_{r+1}}^{(r+1,0)} \\ +r(c_s\nabla_{i_1}-b_{i_1}/c_s)a_{i_2\cdots i_r}^{(r-1,0)}-a_{i_1\cdots i_r}^{(r,1)}\end{array}\right]\mathcal{H}_{i_1\cdots i_r}^{(r)} \\
-\frac{\tau}{R!}\left[\begin{array}{l}\partial a_{i_1\cdots i_R}^{(R,0)}/\partial t-a_{i_1\cdots i_R}^{(R,1)} \\ +R(c_s\nabla_{i_1}-b_{i_1}/c_s)a_{i_2\cdots i_R}^{(R-1,0)}\end{array}\right]\mathcal{H}_{i_1\cdots i_R}^{(R)} \\
-\frac{\tau}{R!}\left(c_s\nabla_{i_1}-\frac{b_{i_1}}{c_s}\right)a_{i_2\cdots i_{R+1}}^{(R,0)}\mathcal{H}_{i_1\cdots i_{R+1}}^{(R+1)}+O(\tau^2)
\end{array}\right\}.
\end{aligned}
\tag{10}
$$

Here, the first term represents the equilibrium distribution $f^{\mathrm{eq},(R,0)}$ associated with the zeroth-order Hilbert expansion, whose coefficients could be obtained by a Hermite expansion of the Maxwellian equilibrium. The second term corresponds to the zeroth-order Hermite polynomial in the first-order Hilbert expansion with the Hermite coefficient recovering the Euler-level continuity equation. The third term involves Hermite polynomials of order $r \geqslant 1$ in the first-order Hilbert expansion, with coefficients linked to the corresponding macroscopic moment equations. Additional terms arise from truncation errors due to the finite $R$th-order Hermite expansion.

Substituting this expansion into the conservation relation Eq. (8) in the generalized CE analysis,

$$
\int [f^{\mathrm{eq},(\infty,0)}-f]\boldsymbol{\psi}d\boldsymbol{\xi} \approx \int [f^{\mathrm{eq},(R,0)}-f^{(R)}]\boldsymbol{\psi}d\boldsymbol{\xi} = \boldsymbol{O}(\tau^2),
\tag{11}
$$

yields the following conditions for the Hermite coefficients:

$$
\frac{\partial}{\partial t}a^{(0,0)}+c_s\nabla\cdot\boldsymbol{a}^{(1,0)}-a^{(0,1)}=O(\tau),
\tag{12}
$$

$$
\begin{aligned}
c_s\frac{\partial}{\partial t}\boldsymbol{a}^{(1,0)}+c_s^2\nabla\cdot(a^{(0,0)}\boldsymbol{I}+\boldsymbol{a}^{(2,0)})-\boldsymbol{b}a^{(0,0)} \\
-c_s\boldsymbol{a}^{(1,1)}=\boldsymbol{O}(\tau),
\end{aligned}
\tag{13}
$$

where $\boldsymbol{I}$ is the identity tensor. The above relations recover the Euler-level macroscopic moment equations obtained from the generalized CE analysis, namely,

$$
\int\left(\frac{Df}{Dt}+\frac{f-f^{\mathrm{eq}}}{\tau}\right)\boldsymbol{\psi}d\boldsymbol{\xi}=\boldsymbol{0},
\tag{14}
$$

with the zeroth-order CE expansion for the distribution function $f=f^{\mathrm{eq},(\infty,0)}+O(\tau)$. This demonstrates that enforcing the NS-level conservation relations is, at the leading order, equivalent to satisfying the incompressible Euler equations. Further analysis of the Euler-level system Eqs. (12) and (13) leads to an acoustic wave equation for the zeroth-order Hermite coefficient $a^{(0,0)}$, namely,

$$
\begin{aligned}
&\frac{\partial^2}{\partial t^2}a^{(0,0)}+\nabla\cdot(c_s\boldsymbol{a}^{(1,1)}+\boldsymbol{b}a^{(0,0)}) \\
&\quad=c_s^2\nabla^2a^{(0,0)}+\frac{\partial}{\partial t}a^{(0,1)}+c_s^2\nabla\nabla:\boldsymbol{a}^{(2,0)}+O(\tau),
\end{aligned}
\tag{15}
$$

which identifies the fundamental origin of spurious acoustic noise in the Boltzmann model equation for incompressible flow simulations.

A first-order CE expansion of the distribution function, $f=f^{\mathrm{eq},(\infty,1)}-\tau Df^{\mathrm{eq},(\infty,0)}/Dt+O(\tau^2)$, substituted into the velocity moment system Eq. (14), yields the NS-level continuity and momentum equations:

$$
\frac{\partial}{\partial t}a^{(0,0)}+\quad c_s\nabla\cdot\boldsymbol{a}^{(1,0)}-a^{(0,1)}-\tau a^{(0,2)}=O(\tau^2),
\tag{16}
$$

$$
\begin{aligned}
c_s\frac{\partial}{\partial t}\boldsymbol{a}^{(1,0)}+\nabla\cdot\left[c_s^2(a^{(0,0)}\boldsymbol{I}+\boldsymbol{a}^{(2,0)})-\boldsymbol{\sigma}\right] \\
-\boldsymbol{b}a^{(0,0)}-c_s(\boldsymbol{a}^{(1,1)}+\tau\boldsymbol{a}^{(1,2)})=\boldsymbol{O}(\tau^2).
\end{aligned}
\tag{17}
$$

And the viscous stress $\boldsymbol{\sigma}$ in Eq. (17) is given by

$$
\begin{aligned}
\boldsymbol{\sigma}&=\int\boldsymbol{cc}\left[f^{\mathrm{eq},(\infty,0)}-f\right]d\boldsymbol{\xi} \\
&=\tau c_s^2\left[\begin{array}{l}\frac{\partial}{\partial t}\boldsymbol{a}^{(2,0)}+c_s\nabla\cdot\boldsymbol{a}^{(3,0)} \\ +c_s(\nabla\boldsymbol{a}^{(1,0)}+(\nabla\boldsymbol{a}^{(1,0)})^T) \\ -\frac{\boldsymbol{b}\boldsymbol{a}^{(1,0)}+\boldsymbol{a}^{(1,0)}\boldsymbol{b}}{c_s}-\boldsymbol{a}^{(2,1)}\end{array}\right]+\boldsymbol{O}(\tau^2),
\end{aligned}
\tag{18}
$$

where the superscript $T$ denotes the transpose of a second-order tensor. Within this generalized CE framework, the Euler equations Eqs. (12) and (13) and the NS equations Eqs. (16) and (17) are consistently recovered. The presence of a hierarchy of Hilbert coefficients provides a systematic avenue to incorporate the higher-order

corrections, providing both flexibility and broad applicability to the formulation.

## III. A UNIFIED KINETIC MODEL FOR INCOMPRESSIBLE FLOWS

We have outlined the formal structure of the generalized CE expansion; its specific expression becomes evident when applied to particular kinetic models. In this paper, we therefore consider incompressible flows, the most widely studied application of the Boltzmann model equation, as a representative case for systematic kinetic analysis. For the NS level, the first-order CE expansion of the distribution function reads

$$f = f^{\mathrm{eq},(\infty,1)} - \tau\left(\frac{\partial}{\partial t} + \boldsymbol{\xi}\cdot\nabla\right) f^{\mathrm{eq},(\infty,0)} - \tau \boldsymbol{b}\cdot\nabla_{\boldsymbol{\xi}} f + O(\tau^2), \tag{19}$$

where the term $\boldsymbol{b}\cdot\nabla_{\boldsymbol{\xi}} f$ represents the contribution of the external force and is treated separately by a Hermite expansion. To achieve accurate incompressible-flow simulations with a minimal particle velocity set, the Hermite expansion is truncated at second order, yielding

$$f^{\mathrm{eq}} \approx f^{\mathrm{eq},(2,1)} = w(\xi, c_s)\begin{bmatrix} (a^{(0,0)} + \tau a^{(0,1)})\mathcal{H}^{(0)} + (\boldsymbol{a}^{(1,0)} + \tau\boldsymbol{a}^{(1,1)} + \tau^2\boldsymbol{a}^{(1,2)}) \\ \cdot\boldsymbol{\mathcal{H}}^{(1)} + (\boldsymbol{a}^{(2,0)} + \tau\boldsymbol{a}^{(2,1)} + \tau^2\boldsymbol{a}^{(2,2)}) : \boldsymbol{\mathcal{H}}^{(2)}/2 \end{bmatrix}, \tag{20}$$

$$\boldsymbol{b}\cdot\nabla_{\boldsymbol{\xi}} f \approx (\boldsymbol{b}\cdot\nabla_{\boldsymbol{\xi}} f)^{(2)} = w(\xi, c_s)\left(\boldsymbol{B}^{(1)}\cdot\boldsymbol{\mathcal{H}}^{(1)} + \frac{1}{2}\boldsymbol{B}^{(2)} : \boldsymbol{\mathcal{H}}^{(2)}\right), \tag{21}$$

where $c_s = \sqrt{RT}$ is a constant for incompressible flows and $\boldsymbol{B}^{(1)}$ and $\boldsymbol{B}^{(2)}$ are the first- and second-order Hermite coefficients for the external force term, respectively. Substituting these expressions into the velocity-moment equations Eq. (14) leads to the NS-level macroscopic system

$$\frac{\partial}{\partial t}a^{(0,0)} + c_s\nabla\cdot\boldsymbol{a}^{(1,0)} - a^{(0,1)} - \tau a^{(0,2)} = 0, \tag{22}$$

$$c_s\frac{\partial}{\partial t}\boldsymbol{a}^{(1,0)} + \nabla\cdot\left[c_s^2(a^{(0,0)}\boldsymbol{I} + \boldsymbol{a}^{(2,0)}) - \boldsymbol{\sigma}\right] + c_s(\boldsymbol{B}^{(1)} - \boldsymbol{a}^{(1,1)} - \tau\boldsymbol{a}^{(1,2)}) = \boldsymbol{0}, \tag{23}$$

where the viscous stress $\boldsymbol{\sigma}$ associated with the external force term is given by

$$\boldsymbol{\sigma} = \int \boldsymbol{cc}[f^{\mathrm{eq},(2,0)} - f]d\boldsymbol{\xi} = \tau c_s^2\begin{bmatrix} \frac{\partial}{\partial t}\boldsymbol{a}^{(2,0)} - \boldsymbol{a}^{(2,1)} + \boldsymbol{B}^{(2)} \\ +c_s(\nabla\boldsymbol{a}^{(1,0)} + (\nabla\boldsymbol{a}^{(1,0)})^T) \end{bmatrix} + \boldsymbol{O}(\tau^2). \tag{24}$$

Moreover, a similar analysis can be conducted at the Euler level, and the corresponding acoustic equation Eq. (15) takes the form

$$\frac{\partial^2}{\partial t^2}a^{(0,0)} + c_s\nabla\cdot(\boldsymbol{a}^{(1,1)} - \boldsymbol{B}^{(1)}) = \frac{\partial}{\partial t}a^{(0,1)} + c_s^2(\nabla^2 a^{(0,0)} + \nabla\nabla : \boldsymbol{a}^{(2,0)}) + O(\tau). \tag{25}$$

And these formulations establish a unified theoretical framework for the systematic analysis and comparison of different kinetic models.

In the following subsections, we examine, within the proposed unified framework, several classical kinetic models for incompressible flows, including the athermal model [29], the He-Luo model [30], the Guo model [31], and the Zhang model [32], and we further introduce the Qi model proposed in this work. In addition, for these kinetic models, we derive a unified on-wall bounce-back boundary condition for the distribution function at the NS level. The detailed derivation of this boundary condition is provided in Appendix B.

Here we clarify two points. First, all kinetic models considered here are weakly compressible, and the term "incompressible" refers to the target macroscopic regime recovered in the low-Mach-number limit rather than a strict kinetic constraint. Second, the athermal, He-Luo, Guo, and Zhang models satisfy $\boldsymbol{a}^{(r,q)} = \boldsymbol{0}$ for $q \geqslant 1$, corresponding to $Q = 0$ in Eq. (6); their equilibria are independent of $\tau$ and thus belong to the hierarchy of Shan *et al.* [16]. In contrast, the Qi model introduced in Sec. III D has nonzero $\boldsymbol{a}^{(0,1)}$ and $\boldsymbol{a}^{(2,1)}$, requiring $Q \geqslant 1$ and as such extending beyond this hierarchy.

### A. The athermal model

The first model considered here is the athermal model [29], which is obtained directly by performing a Hermite expansion of the exponential equilibrium $f^{\mathrm{eq}} = \rho(2\pi RT)^{-3/2}\exp[-c^2/(2RT)]$ to the second order. Within this framework, the Hilbert coefficients and the Hermite coefficients for the external force term are explicitly given by

$$a^{(0,0)} = \rho, \quad \boldsymbol{a}^{(1,0)} = \rho\frac{\boldsymbol{u}}{c_s}, \quad \boldsymbol{a}^{(2,0)} = \rho\frac{\boldsymbol{uu}}{c_s^2}, \tag{26}$$

$$a^{(0,1)} = a^{(0,2)} = 0, \quad \boldsymbol{a}^{(1,1)} = \boldsymbol{a}^{(1,2)} = \boldsymbol{a}^{(2,1)} = \boldsymbol{a}^{(2,2)} = \boldsymbol{0}, \tag{27}$$

$$\boldsymbol{B}^{(1)} = -\rho\frac{\boldsymbol{b}}{c_s}, \quad \boldsymbol{B}^{(2)} = -\rho\frac{\boldsymbol{bu} + \boldsymbol{ub}}{c_s^2}. \tag{28}$$

And the equilibrium for the athermal model may be expressed as

$$f^{\mathrm{eq}} = \rho w(\xi, c_s)\left\{1 + \frac{\boldsymbol{u}\cdot\boldsymbol{\xi}}{c_s^2} + \frac{1}{2}\left[\left(\frac{\boldsymbol{u}\cdot\boldsymbol{\xi}}{c_s^2}\right)^2 - \frac{u^2}{c_s^2}\right]\right\}. \tag{29}$$

The corresponding NS-level macroscopic moment equations read

$$\frac{\partial}{\partial t}\rho + \nabla\cdot(\rho\boldsymbol{u}) = 0, \tag{30}$$

$$\frac{\partial}{\partial t}(\rho \boldsymbol{u}) + \nabla \cdot \left(c_s^2 \rho \boldsymbol{I} + \rho \boldsymbol{u}\boldsymbol{u} - \boldsymbol{\sigma}\right) = \rho \boldsymbol{b}, \tag{31}$$

with the viscous stress given by

$$\begin{aligned}\boldsymbol{\sigma} &= \tau \left[ \frac{\partial}{\partial t}(\rho \boldsymbol{u}\boldsymbol{u}) - \rho(\boldsymbol{b}\boldsymbol{u} + \boldsymbol{u}\boldsymbol{b}) + c_s^2 \nabla(\rho \boldsymbol{u}) + c_s^2 [\nabla(\rho \boldsymbol{u})]^T \right] \\ &\quad + \boldsymbol{O}(\tau^2) \\ &= \tau \rho c_s^2 [\nabla \boldsymbol{u} + (\nabla \boldsymbol{u})^T] - \tau \nabla \cdot (\rho \boldsymbol{u}\boldsymbol{u}\boldsymbol{u}) + \boldsymbol{O}(\tau^2),\end{aligned} \tag{32}$$

where $\tau c_s^2$ is equal to the kinematic viscosity $\nu$. Here $\nabla \cdot (\rho \boldsymbol{u}\boldsymbol{u}\boldsymbol{u})$ denotes an error term of $O(\mathrm{Ma}^3)$ where Ma is the Mach number, arising from truncation of the Hermite expansion of the exponential equilibrium. This error vanishes if a sufficiently high order is retained in the Hermite expansion, such that the third-order coefficient satisfies $a^{(3,0)} = \rho \boldsymbol{u}\boldsymbol{u}\boldsymbol{u}/c_s^3$. Furthermore, the resulting acoustic equation recovered by this model is

$$\frac{\partial^2 \rho}{\partial t^2} = c_s^2 \nabla^2 \rho + \nabla\nabla : (\rho \boldsymbol{u}\boldsymbol{u}) - \nabla \cdot (\rho \boldsymbol{b}) + O(\tau), \tag{33}$$

which coincides with the acoustic equation for the athermal flows [42].

### B. The He-Luo model

The second model considered is the He-Luo model [30], which can be obtained directly from the athermal model by decomposing the density into a mean component $\rho_0$ and a fluctuation $\delta\rho$. Within the present framework, the Hilbert coefficients and the Hermite coefficients for the external force term take the form

$$a^{(0,0)} = \delta\rho, \quad \boldsymbol{a}^{(1,0)} = \rho_0 \frac{\boldsymbol{u}}{c_s}, \quad \boldsymbol{a}^{(2,0)} = \rho_0 \frac{\boldsymbol{u}\boldsymbol{u}}{c_s^2}, \tag{34}$$

$$a^{(0,1)} = a^{(0,2)} = 0, \quad \boldsymbol{a}^{(1,1)} = \boldsymbol{a}^{(1,2)} = \boldsymbol{a}^{(2,1)} = \boldsymbol{a}^{(2,2)} = \boldsymbol{0}, \tag{35}$$

$$\boldsymbol{B}^{(1)} = -\rho_0 \frac{\boldsymbol{b}}{c_s}, \quad \boldsymbol{B}^{(2)} = -\rho_0 \frac{\boldsymbol{b}\boldsymbol{u} + \boldsymbol{u}\boldsymbol{b}}{c_s^2}. \tag{36}$$

And the equilibrium for the He-Luo model can be given as

$$f^{\mathrm{eq}} = w(\xi, c_s) \left\{ \delta\rho + \rho_0 \frac{\boldsymbol{u}\cdot\boldsymbol{\xi}}{c_s^2} + \frac{\rho_0}{2} \left[ \left( \frac{\boldsymbol{u}\cdot\boldsymbol{\xi}}{c_s^2} \right)^2 - \frac{u^2}{c_s^2} \right] \right\}. \tag{37}$$

The corresponding NS-level moment equations are

$$\frac{\partial \delta\rho}{\partial t} + \rho_0 \nabla \cdot \boldsymbol{u} = 0, \tag{38}$$

$$\rho_0 \frac{\partial \boldsymbol{u}}{\partial t} + \nabla \cdot \left(c_s^2 \delta\rho \boldsymbol{I} + \rho_0 \boldsymbol{u}\boldsymbol{u} - \boldsymbol{\sigma}\right) = \rho_0 \boldsymbol{b}, \tag{39}$$

with the viscous stress given as

$$\begin{aligned}\boldsymbol{\sigma} &= \tau \rho_0 c_s^2 [\nabla \boldsymbol{u} + (\nabla \boldsymbol{u})^T] \\ &\quad + \tau \rho_0 \left[ \frac{\partial(\boldsymbol{u}\boldsymbol{u})}{\partial t} - \boldsymbol{b}\boldsymbol{u} - \boldsymbol{u}\boldsymbol{b} \right] + \boldsymbol{O}(\tau^2) \\ &= \tau \rho_0 c_s^2 [\nabla \boldsymbol{u} + (\nabla \boldsymbol{u})^T] - \tau c_s^2 [\boldsymbol{u}\nabla\delta\rho + (\boldsymbol{u}\nabla\delta\rho)^T] \\ &\quad - \tau \rho_0 [\boldsymbol{u}\boldsymbol{u}\cdot\nabla\boldsymbol{u} + (\boldsymbol{u}\boldsymbol{u}\cdot\nabla\boldsymbol{u})^T] + 2\tau \boldsymbol{u}\boldsymbol{u} \frac{\partial \delta\rho}{\partial t} + \boldsymbol{O}(\tau^2),\end{aligned} \tag{40}$$

where the second equality follows from the macroscopic moment equations and the last three terms in the last equation are model errors of $O(\mathrm{Ma}^3)$. In contrast to the athermal model, these errors cannot be eliminated by increasing the order of the Hermite expansion of the equilibrium.

At the Euler level, the recovered acoustic equation reads

$$\frac{\partial^2 \delta\rho}{\partial t^2} = c_s^2 \nabla^2 \delta\rho + \rho_0 \nabla\nabla : (\boldsymbol{u}\boldsymbol{u}) - \rho_0 \nabla \cdot \boldsymbol{b} + O(\tau). \tag{41}$$

In the absence of external force and for a quiescent flow ($\boldsymbol{u} = \boldsymbol{0}$ and $\boldsymbol{b} = \boldsymbol{0}$), this equation has a traveling-wave solution

$$\delta\rho = C \exp\left[i(\boldsymbol{k}_w \cdot \boldsymbol{x} \pm c_s |\boldsymbol{k}_w| t)\right], \tag{42}$$

where $C$ is a constant and $\boldsymbol{k}_w$ is the wave vector. This behavior indicates the lack of an effective dissipation mechanism for density fluctuations in the He-Luo model, leading to pronounced numerical oscillations in the hydrodynamic pressure $p = c_s^2 \delta\rho$, which constitutes an intrinsic limitation of the model for incompressible simulations.

### C. The Guo model and the Zhang model

We consider the Guo and Zhang models [31,32] together, as they recover identical macroscopic equations and differ only in the construction of the equilibrium distribution: the Guo model prescribes distinct equilibria for different discrete velocities, whereas the Zhang model employs a unified Hermite expansion. For brevity, we detail the analysis for the Zhang model; the Guo model follows analogously and is summarized at the end of this subsection.

For the Zhang model [32], the Hilbert coefficients and the Hermite coefficients for the external force term read

$$a^{(0,0)} = \rho_0, \quad \boldsymbol{a}^{(1,0)} = \rho_0 \frac{\boldsymbol{u}}{c_s}, \quad \boldsymbol{a}^{(2,0)} = \rho_0 \frac{\boldsymbol{u}\boldsymbol{u}}{c_s^2} + \left( \frac{p}{c_s^2} - \rho_0 \right) \boldsymbol{I}, \tag{43}$$

$$a^{(0,1)} = a^{(0,2)} = 0, \quad \boldsymbol{a}^{(1,1)} = \boldsymbol{a}^{(1,2)} = \boldsymbol{a}^{(2,1)} = \boldsymbol{a}^{(2,2)} = \boldsymbol{0}, \tag{44}$$

$$\boldsymbol{B}^{(1)} = -\rho_0 \frac{\boldsymbol{b}}{c_s}, \quad \boldsymbol{B}^{(2)} = -\rho_0 \frac{\boldsymbol{b}\boldsymbol{u} + \boldsymbol{u}\boldsymbol{b}}{c_s^2}, \tag{45}$$

where $p$ is the hydrodynamic pressure. Consequently, the equilibrium for the Zhang model can be represented as

$$\begin{aligned}f^{\mathrm{eq}} = w(\xi, c_s) \Bigg\{ &\rho_0 + \rho_0 \frac{\boldsymbol{u}\cdot\boldsymbol{\xi}}{c_s^2} + \frac{\rho_0}{2} \left[ \left( \frac{\boldsymbol{u}\cdot\boldsymbol{\xi}}{c_s^2} \right)^2 - \frac{u^2}{c_s^2} \right] \\ &+ \left( \frac{p}{c_s^2} - \rho_0 \right) \left( \frac{\xi^2}{2c_s^2} - \frac{D}{2} \right) \Bigg\},\end{aligned} \tag{46}$$

where $D$ is the dimension for the spatial coordinate $\boldsymbol{x}$. In the Zhang model, hydrodynamic pressure $p$ is represented in the second-order Hermite coefficient of the equilibrium distribution, indicating that pressure as well as momentum

are regarded as conserved variables. This may not correspond with the true physics of incompressible fluids.

The NS-level equations for the Zhang model are

$$\rho_0 \nabla \cdot \boldsymbol{u} = O(\tau^2), \tag{47}$$

$$\rho_0 \frac{\partial \boldsymbol{u}}{\partial t} + \nabla \cdot (\rho_0 \boldsymbol{uu} + p\boldsymbol{I} - \boldsymbol{\sigma}) = \rho_0 \boldsymbol{b}. \tag{48}$$

As implied by Eq. (47), incompressibility of the velocity field is enforced only at the NS level, and there are higher-order residual errors. The viscous stress $\boldsymbol{\sigma}$ takes the form

$$\begin{aligned}\boldsymbol{\sigma} &= \tau \rho_0 c_s^2 [\nabla \boldsymbol{u} + (\nabla \boldsymbol{u})^T] + \tau \left[ \frac{\partial}{\partial t} (\rho_0 \boldsymbol{uu} + p\boldsymbol{I}) \right. \\ &\quad \left. - \rho_0 (\boldsymbol{bu} + \boldsymbol{ub}) \right] + \boldsymbol{O}(\tau^2) \\ &= \tau \rho_0 c_s^2 [\nabla \boldsymbol{u} + (\nabla \boldsymbol{u})^T] - \tau c_s^2 [\boldsymbol{u} \nabla \delta\rho + (\boldsymbol{u} \nabla \delta\rho)^T] \\ &\quad - \tau \rho_0 [\boldsymbol{uu} \cdot \nabla \boldsymbol{u} + (\boldsymbol{uu} \cdot \nabla \boldsymbol{u})^T] + \tau \frac{\partial p}{\partial t} \boldsymbol{I} + \boldsymbol{O}(\tau^2), \end{aligned} \tag{49}$$

where the second equality is derived from the macroscopic moment equations and the last three terms in the last equation are model errors that cannot be eliminated by increasing the Hermite order. Notably, only the last term in Eq. (49) differs from that in Eq. (40) for the He-Luo model: it is proportional to the temporal derivative of the local hydrodynamic pressure, rather than to the temporal derivative of coupled velocity and density fluctuation, leading to distinct behavior in the recovered viscous stress.

For the Zhang model, the zeroth-order Hermite coefficient $a^{(0,0)}$ is prescribed as a constant rather than treated as a dynamical variable. Consequently, at the Euler level the acoustic wave equation for $a^{(0,0)}$ in Eq. (15) no longer involves its time derivative. Instead, it reduces to a pressure Poisson equation,

$$\nabla\nabla : (\rho_0 \boldsymbol{uu} + p\boldsymbol{I}) - \rho_0 \nabla \cdot \boldsymbol{b} = O(\tau), \tag{50}$$

which is consistent with the role of hydrodynamic pressure in incompressible flows. However, since the velocity is not guaranteed to be divergence free, higher-order dilatational velocity components at $O(\tau^2)$ may still contaminate the hydrodynamic pressure through this relation.

For the Guo model [31], we adopt

$$f^{\mathrm{eq}} = \begin{cases} -\frac{p}{c_s^2} + \frac{w(\xi, c_s)}{c_s^2} \left\{ p + \rho_0 \left[ \boldsymbol{u} \cdot \boldsymbol{\xi} + \frac{\boldsymbol{uu}}{2} : \left( \frac{\boldsymbol{\xi\xi}}{c_s^2} - \boldsymbol{I} \right) \right] \right\} & \text{for} \quad \boldsymbol{\xi} = \boldsymbol{0}, \\ \frac{w(\xi, c_s)}{c_s^2} \left\{ p + \rho_0 \left[ \boldsymbol{u} \cdot \boldsymbol{\xi} + \frac{\boldsymbol{uu}}{2} : \left( \frac{\boldsymbol{\xi\xi}}{c_s^2} - \boldsymbol{I} \right) \right] \right\} & \text{for} \quad \boldsymbol{\xi} \neq \boldsymbol{0}, \end{cases} \tag{51}$$

and the analysis proceeds in the same manner. The recovered macroscopic equations, viscous stress, and pressure Poisson equation are identical to those of the Zhang model; the detailed derivation is therefore omitted for conciseness.

### D. Present model (the Qi model)

To remedy the lack of numerical damping for density fluctuations in the He-Luo model [30], we propose a formulation, hereafter referred to as the Qi model. As in the He-Luo model, the density is decomposed into a mean component $\rho_0$ and a fluctuation $\delta\rho$, preserving a clear physical interpretation. The key modification is the introduction of an oscillation-suppression term $\chi \delta\rho$, where $\chi$ is a tunable parameter designed to attenuate spurious oscillations; its admissible range is determined below.

The Hilbert coefficients and Hermite coefficients for the external force term are

$$\begin{aligned} a^{(0,0)} &= \delta\rho, \quad \boldsymbol{a}^{(1,0)} = \rho_0 \frac{\boldsymbol{u}}{c_s}, \\ \boldsymbol{a}^{(2,0)} &= \rho_0 \frac{\boldsymbol{uu}}{c_s^2}, \quad a^{(0,1)} = \chi \delta\rho, \end{aligned} \tag{52}$$

$$a^{(0,2)} = 0, \quad \boldsymbol{a}^{(1,1)} = \boldsymbol{a}^{(1,2)} = \boldsymbol{a}^{(2,2)} = \boldsymbol{0},$$

$$\boldsymbol{a}^{(2,1)} = -2\chi \delta\rho \frac{\boldsymbol{uu}}{c_s^2}, \tag{53}$$

$$\boldsymbol{B}^{(1)} = -\rho_0 \frac{\boldsymbol{b}}{c_s}, \quad \boldsymbol{B}^{(2)} = -\rho_0 \frac{\boldsymbol{bu} + \boldsymbol{ub}}{c_s^2}, \tag{54}$$

and the model degenerates to the He-Luo formulation when $\chi = 0$. Thus, the equilibrium distribution for the Qi model is

$$\begin{aligned} f^{\mathrm{eq}} = w(\xi, c_s) \Bigg\{ & \delta\rho (1 + \tau\chi) + \rho_0 \frac{\boldsymbol{u} \cdot \boldsymbol{\xi}}{c_s^2} \\ & + \left( \frac{\rho_0}{2} - \tau \chi \delta\rho \right) \left[ \left( \frac{\boldsymbol{u} \cdot \boldsymbol{\xi}}{c_s^2} \right)^2 - \frac{u^2}{c_s^2} \right] \Bigg\}. \end{aligned} \tag{55}$$

The macroscopic moment equations at the NS level are

$$\frac{\partial \delta\rho}{\partial t} + \rho_0 \nabla \cdot \boldsymbol{u} = \chi \delta\rho, \tag{56}$$

$$\rho_0 \frac{\partial \boldsymbol{u}}{\partial t} + \nabla \cdot \left( c_s^2 \delta\rho \boldsymbol{I} + \rho_0 \boldsymbol{uu} - \boldsymbol{\sigma} \right) = \rho_0 \boldsymbol{b}, \tag{57}$$

where the treatment of the incompressible continuity equation adopted here is mathematically equivalent to a hybrid strategy combining both the artificial compressibility [33] and the penalty parameter [40]. The viscous stress $\boldsymbol{\sigma}$ is

$$\begin{aligned} \boldsymbol{\sigma} &= \tau \rho_0 c_s^2 [\nabla \boldsymbol{u} + (\nabla \boldsymbol{u})^T] + \tau \rho_0 \left[ \frac{\partial (\boldsymbol{uu})}{\partial t} - (\boldsymbol{bu} + \boldsymbol{ub}) \right] \\ &\quad + 2\tau \chi \delta\rho \boldsymbol{uu} + \boldsymbol{O}(\tau^2) \\ &= \tau \rho_0 c_s^2 [\nabla \boldsymbol{u} + (\nabla \boldsymbol{u})^T] - \tau c_s^2 [\boldsymbol{u} \nabla \delta\rho + (\boldsymbol{u} \nabla \delta\rho)^T] \\ &\quad - \tau \rho_0 [\boldsymbol{uu} \cdot \nabla \boldsymbol{u} + (\boldsymbol{uu} \cdot \nabla \boldsymbol{u})^T] + 2\tau \boldsymbol{uu} \frac{\partial \delta\rho}{\partial t} + \boldsymbol{O}(\tau^2), \end{aligned} \tag{58}$$

where the second equality is obtained by the macroscopic moment equations and the last three terms in the final equation coincide with those of the He-Luo model, implying that

the Qi model does not introduce larger errors for the viscous stress. The additional term $2\tau\chi\delta\rho\boldsymbol{uu}$ in the first line originates from the $-\boldsymbol{a}^{(2,1)}$ contribution in Eq. (24). Using the modified continuity equation, this contribution is exactly canceled by the time-derivative term in $\tau\rho_0\partial(\boldsymbol{uu})/\partial t$. Hence, the Qi and He-Luo models yield the same viscous stress, Eq. (40), up to $O(\tau^2)$. Moreover, effective suppression of spurious oscillations reduces the contribution of $\partial\delta\rho/\partial t$ to the viscous stress.

We conduct a further analysis of the acoustic wave equation pertaining to the density perturbation $\delta\rho$ in the Qi model. For the density fluctuation, the corresponding acoustic equation becomes

$$\frac{\partial^2\delta\rho}{\partial t^2} = \chi\frac{\partial\delta\rho}{\partial t} + c_s^2\nabla^2\delta\rho + \nabla\nabla : (\rho_0\boldsymbol{uu}) - \rho_0\nabla\cdot\boldsymbol{b} + O(\tau). \tag{59}$$

For a quiescent flow without forcing ($\boldsymbol{u}=\boldsymbol{0}$ and $\boldsymbol{b}=\boldsymbol{0}$), the equation admits the traveling-wave solution

$$\delta\rho = C\exp\left[i\boldsymbol{k}_w\cdot\boldsymbol{x} + \frac{t}{2}\left(\chi \pm \sqrt{\chi^2 - 4c_s^2|\boldsymbol{k}_w|^2}\right)\right] \approx C\exp\left[i(\boldsymbol{k}_w\cdot\boldsymbol{x} \pm c_s|\boldsymbol{k}_w|t) + \frac{t}{2}\chi\right]. \tag{60}$$

Here we note that a negative $\chi$ provides exponential damping of spurious oscillations; however, excessively large negative values would violate the asymptotic consistency of the Hilbert expansion in the relaxation time $\tau$. Consequently, $\chi$ should satisfy $\chi\sim O(1)$ with $\chi\leqslant 0$.

## IV. MESOSCOPIC SIMULATIONS OF THREE-DIMENSIONAL INCOMPRESSIBLE DECAYING TURBULENCE

To enable a systematic comparison of the kinetic models discussed in Sec. III, incompressible decaying turbulence is considered as a benchmark case. All simulations are performed using the discrete unified gas-kinetic scheme (DUGKS) [14], a finite-volume Boltzmann solver, with numerical implementation following Qi *et al.* [43,44]; a brief description of the method is provided in Appendix C. DUGKS permits an *off-lattice* configuration for the particle velocity space, decoupling particle velocities from the physical space grid. The distribution function is discretized using the three-dimensional D3V13A5 velocity set [16,45], which achieves fifth-order Gauss-Hermite quadrature accuracy with only 13 discrete velocities. To the best of our knowledge, this constitutes the minimal velocity set currently available for three-dimensional incompressible-flow simulations within a mesoscopic framework. The corresponding weights and abscissae of this velocity set are provided in Appendix D.

The choice of decaying turbulence is motivated by three considerations. First, for an artificial compressibility method, the hydrodynamic pressure and spurious acoustic pressure decay on distinct timescales, allowing the numerical noise to be apparently separated at later stages [38,41]. Second, incompressible decaying turbulence admits accurate reference results from pseudospectral (PS) methods [46], in which the velocity field is strictly divergence free, facilitating quantitative validation. Third, this configuration is well suited to Helmholtz-Hodge decomposition [47,48] in the spectral space, enabling a clear separation of solenoidal and dilatational velocity components induced by artificial compressibility, which is essential for the subsequent analysis.

In addition, to assess the performance of the different models in wall-bounded flows, Appendix E presents simulations of the two-dimensional lid-driven cavity flow. These two-dimensional computations are performed using the same DUGKS implementation, but with the velocity space discretized by the *on-lattice* D2Q9A5 velocity set, which consists of nine discrete velocities and is also detailed in Appendix D. For brevity, the main text focuses on the three-dimensional incompressible decaying turbulence simulations.

### A. Problem statement and parameter settings

The decaying turbulence simulations are conducted in a periodic cubic domain of size $L^3 = 2\pi^3$, discretized using a uniform Cartesian grid. For the PS case, the reference density is set to $\rho_0 = 1.0$. And the initial condition is prescribed as an incompressible Gaussian random velocity field with a given radial kinetic energy spectrum $E(k, t=0)$ in spectral space. An inverse Fourier transform is then applied to obtain a divergence-free velocity field $\boldsymbol{u}(\boldsymbol{x}, t=0)$ in physical space. Specifically, the initial energy spectrum is given by

$$E(k,t=0) = \begin{cases} A_0k^4\exp\left(-2k^2/k_0^2\right), & \text{for} \quad 3\leqslant k\leqslant 8, \\ 0, & \text{for} \quad \text{others}, \end{cases} \tag{61}$$

where $k$ denotes the wave-number magnitude for the wave number $\boldsymbol{k}$, $A_0 = 2\times10^{-3}$, and $k_0 = 4$. All DUGKS simulations use exactly the same initial velocity field as the PS case, while the corresponding initial pressure and density fluctuations are obtained by solving the pressure Poisson equation associated with the given velocity field.

For incompressible decaying turbulence, a detailed assessment of flow statistics and energy spectra obtained with a mesoscopic approach (MRT-LBE) was reported by Qi *et al.* [38]. And the study showed that the pressure, dilatation (velocity divergence), and dilatational velocity component are the quantities most strongly affected by artificial compressibility effects. Accordingly, the present work focuses on a subset of representative statistics that are particularly sensitive to these effects. The turbulent kinetic energy $K$, dissipation rate $\epsilon$, and root-mean-square (rms) velocity $u_{\rm rms}$ are defined as

$$K = \frac{\langle\boldsymbol{u}\cdot\boldsymbol{u}\rangle}{2}, \quad \epsilon = 2\nu\langle S_{ij}S_{ij}\rangle, \quad u_{\rm rms} = \sqrt{\frac{\langle\boldsymbol{u}\cdot\boldsymbol{u}\rangle}{3}}, \tag{62}$$

where $\langle\cdots\rangle$ denotes spatial averaging, $\boldsymbol{S} = [\nabla\boldsymbol{u} + (\nabla\boldsymbol{u})^T]/2$ is the strain rate tensor, and we note that all the derivatives in the postprocessing are calculated in the spectral space to achieve exponential accuracy. The Kolmogorov length scale $\eta$, the Taylor microscale $\lambda$, the Taylor microscale Reynolds number $\mathrm{Re}_\lambda$, the turbulent Mach number $\mathrm{Ma}_t$,

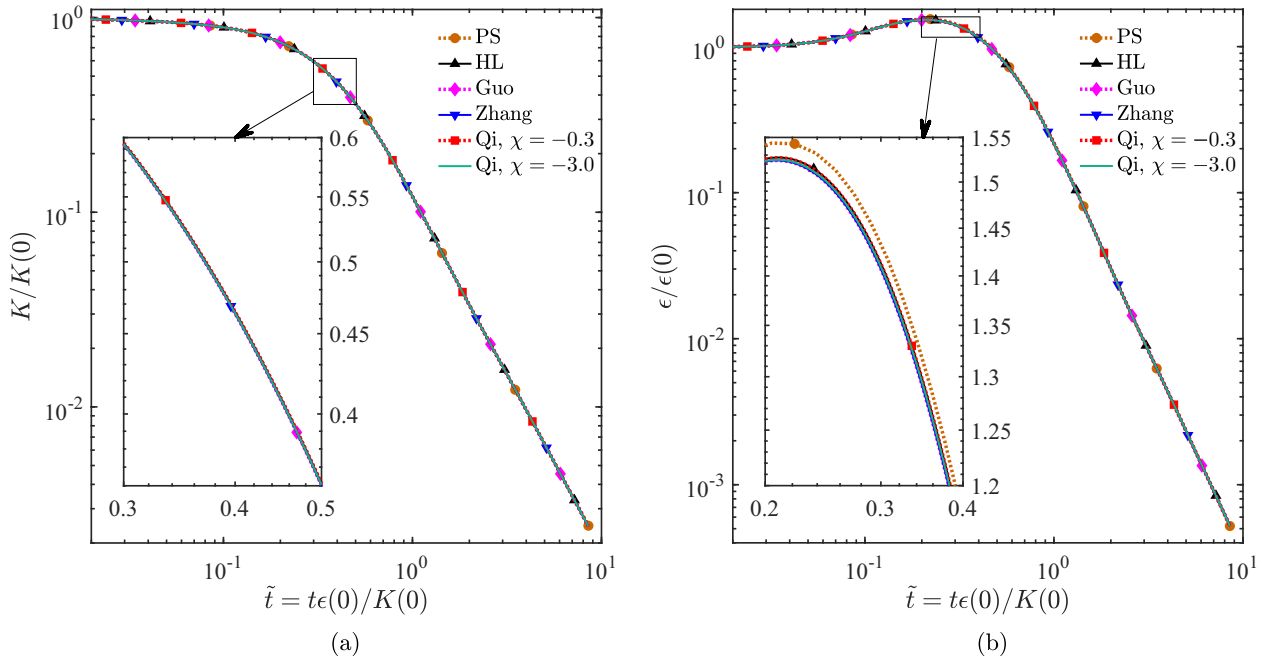



FIG. 1. Evolutions of (a) the normalized turbulent kinetic energy $K/K(0)$ and (b) the normalized dissipation rate $\epsilon/\epsilon(0)$ for $\mathrm{Re}_{\lambda,0} = 49.02$. "PS" denotes the reference data calculated by the PS method, and "HL" represents the He-Luo model.

the rms dilatation $\vartheta_{\mathrm{rms}}$, and the rms pressure $p_{\mathrm{rms}}$ are as follows:

$$\eta = \left(\frac{\nu^3}{\epsilon}\right)^{1/4},$$

$$\lambda = \frac{\sqrt{3}u_{\mathrm{rms}}}{\sqrt{\langle(\partial u_x/\partial x)^2 + (\partial u_y/\partial y)^2 + (\partial u_z/\partial z)^2\rangle}}, \tag{63}$$

$$\mathrm{Re}_\lambda = \frac{u_{\mathrm{rms}}\lambda}{\nu}, \quad \mathrm{Ma}_t = \frac{u_{\mathrm{rms}}}{c_s},$$

$$\vartheta_{\mathrm{rms}} = \sqrt{\vartheta^2}, \quad p_{\mathrm{rms}} = \sqrt{(p-p_0)^2}, \tag{64}$$

where $\vartheta = \nabla\cdot\boldsymbol{u}$ is the dilatation and $p_0 = \rho_0 c_s^2$ is the reference pressure. The solenoidal velocity $\boldsymbol{u}_s$ and the dilatational velocity $\boldsymbol{u}_d$ are determined in the spectral space, i.e.,

$$\widehat{\boldsymbol{u}}_s(\boldsymbol{k},t) = \widehat{\boldsymbol{u}}(\boldsymbol{k},t) - \frac{\widehat{\boldsymbol{u}}(\boldsymbol{k},t)\cdot\boldsymbol{k}}{k^2}\boldsymbol{k}, \quad \widehat{\boldsymbol{u}}_d(\boldsymbol{k},t) = \frac{\widehat{\boldsymbol{u}}(\boldsymbol{k},t)\cdot\boldsymbol{k}}{k^2}\boldsymbol{k}, \tag{65}$$

where $\widehat{(\cdots)}$ denotes the converted physical variable in the $\boldsymbol{k}$ spectral space. And the rms solenoidal velocity $u_{s,\mathrm{rms}}$ and the rms dilatational velocity $u_{d,\mathrm{rms}}$ are evaluated by

$$u_{s,\mathrm{rms}} = \sqrt{\frac{\langle\boldsymbol{u}_s\cdot\boldsymbol{u}_s\rangle}{3}}, \quad u_{d,\mathrm{rms}} = \sqrt{\frac{\langle\boldsymbol{u}_d\cdot\boldsymbol{u}_d\rangle}{3}}. \tag{66}$$

Furthermore, the velocity-derivative skewness $S_u$ and flatness $F_u$ averaged over three directions are

$$S_u = \frac{\langle[(\partial u_x/\partial x)^3 + (\partial u_y/\partial y)^3 + (\partial u_z/\partial z)^3]/3\rangle}{\langle[(\partial u_x/\partial x)^2 + (\partial u_y/\partial y)^2 + (\partial u_z/\partial z)^2]/3\rangle^{3/2}}, \tag{67}$$

$$F_u = \frac{\langle[(\partial u_x/\partial x)^4 + (\partial u_y/\partial y)^4 + (\partial u_z/\partial z)^4]/3\rangle}{\langle[(\partial u_x/\partial x)^2 + (\partial u_y/\partial y)^2 + (\partial u_z/\partial z)^2]/3\rangle^2}. \tag{68}$$

Based on the parameter study of Qi *et al.* [38] concerning the effects of the initial Mach number, grid resolution, and bulk viscosity, we compare the aforementioned kinetic models by considering two representative cases with different initial Reynolds numbers. All simulations employ the same prescribed initial energy spectrum Eq. (61), yielding an initial rms velocity $u_{\mathrm{rms},0} = 1.036$. In the DUGKS framework, the reference sound speed is fixed at $c_s = 14.17$, so that the initial turbulent Mach number is identical for all cases, $\mathrm{Ma}_{t,0} = 0.073\,13$.

In case 1, the initial Taylor-scale Reynolds number is $\mathrm{Re}_{\lambda,0} = 49.02$, with kinematic viscosity $\nu = 1.040\times10^{-2}$, time step $\Delta t = 8\times10^{-4}$, and a uniform grid of $256^3$. Although the Kolmogorov length scale $\eta$ evolves in time, the spatial resolution always satisfies $k_{\max}\eta \geqslant 4.072$, which is sufficient to resolve all small-scale structures in the incompressible turbulence [38,49].

Case 2 corresponds to a higher Reynolds number, $\mathrm{Re}_{\lambda,0} = 95.36$, obtained with $\nu = 5.400\times10^{-3}$. The time step is reduced to $\Delta t = 3\times10^{-4}$, and the grid is refined to $384^3$. For this case, the resolution criterion $k_{\max}\eta \geqslant 3.938$ is maintained throughout the simulation, ensuring adequate grid convergence.

As the athermal model exhibits the worst performance in suppressing spurious acoustic noise, its results are omitted from the subsequent contents. The discussions that follow therefore focus on the He-Luo, Guo, and Zhang models; two Qi-model variants with $\chi = -0.3$ and $-3.0$; and the PS method used as a reference.

### B. Temporal evolution of turbulent statistics

This subsection examines the temporal evolution of key flow statistics predicted by the different kinetic models. Figure 1 shows the results for the lower-resolution case $\mathrm{Re}_{\lambda,0} = 49.02$. As shown in Fig. 1(a), the normalized kinetic energy decays monotonically, and all kinetic models yield virtually

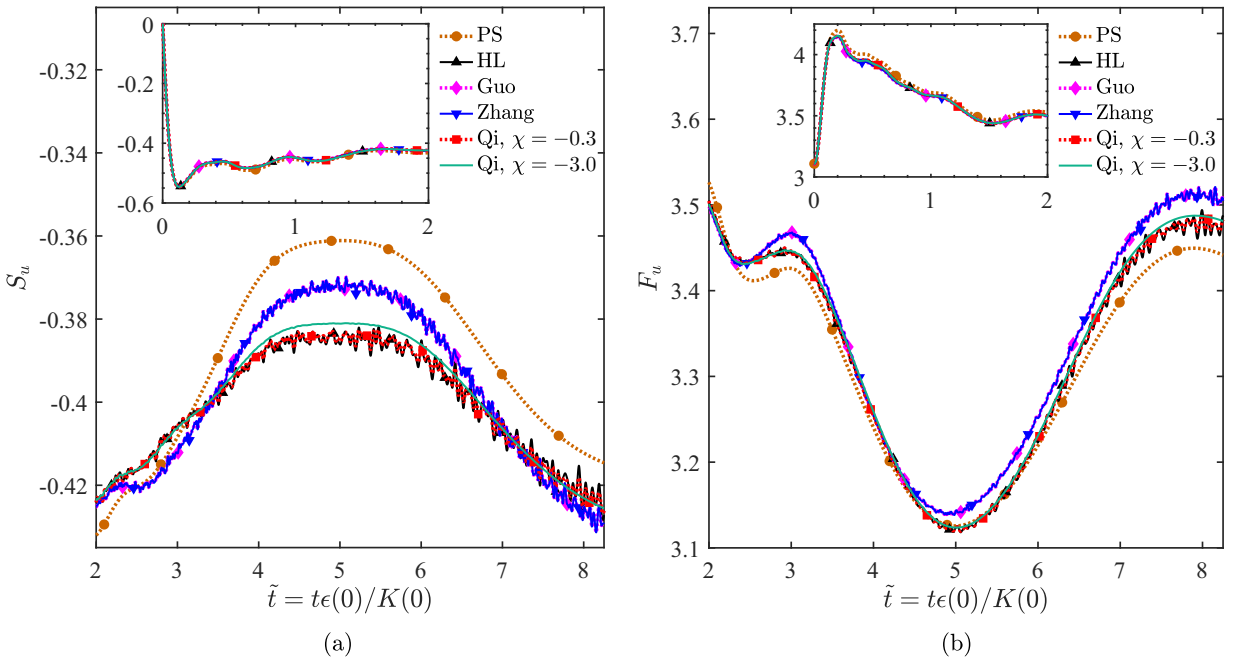



FIG. 2. Evolutions of the velocity-derivative (a) skewness $S_u$ and (b) flatness $F_u$ for $\mathrm{Re}_{\lambda,0} = 49.02$.

indistinguishable results. The dissipation rate in Fig. 1(b) increases as small-scale vortical structures develop, reaches a maximum at normalized times $0.2 < \tilde{t} < 0.3$, and then decays. Again, the predictions of the kinetic models collapse closely onto one another, with only minor deviations from the PS result. The higher-resolution case $\mathrm{Re}_{\lambda,0} = 95.36$ exhibits the same qualitative behavior for both kinetic energy and dissipation rate and is therefore not discussed further.

We next examine higher-order statistics that characterize small-scale turbulent dynamics, namely the skewness associated with vortex stretching, and the flatness reflecting turbulent intermittency. Figure 2 presents the temporal evolution of these quantities for the case $\mathrm{Re}_{\lambda,0} = 49.02$. The skewness decreases from zero to approximately $-0.5$, while the flatness increases from zero to about 4.2 before gradually decaying. During the early stage ($\tilde{t} < 1.5$), all models yield nearly identical results. At later times, discrepancies emerge both among the kinetic models and between the mesoscopic and PS curves. Notably, the Guo and Zhang models produce almost indistinguishable curves, both exhibiting pronounced oscillations induced by spurious noise. By contrast, the Qi model with $\chi = -0.3$ follows the overall trend of the He-Luo model while partially suppressing these oscillations. When $\chi$ is reduced to $-3.0$, the Qi model effectively eliminates the spurious oscillations in both skewness and flatness, yielding results that lie between those of the He-Luo and PS curves. For models lacking an explicit noise-damping mechanism, the oscillation amplitude increases with time, indicating that the decay timescale of spurious noise exceeds that of the turbulent kinetic energy.

For the case with an increased initial Reynolds number $\mathrm{Re}_\lambda = 95.36$, the temporal evolutions of skewness and flatness are shown in Fig. 3. The peak skewness remains close to $-0.5$, whereas the peak flatness increases to about 4.7, indicating enhanced intermittency at higher Reynolds numbers. All methods yield nearly identical results during the first two nondimensional times, after which noticeable discrepancies emerge. The behaviors of the Zhang and Guo models, as well as of the Qi model with different values of $\chi$, closely mirror those observed in Fig. 2. Across both $\mathrm{Re}_{\lambda,0}$ cases, the results consistently indicate that the Qi model significantly mitigates the impact of spurious noise on small-scale turbulent dynamics for moderate $\chi$, and completely suppresses such noise when $|\chi|$ is sufficiently large.

Figure 4 shows the temporal evolution of the rms pressure for different Reynolds numbers. Overall, the rms pressure exhibits an approximate power-law decay. Beyond a nondimensional time $\tilde{t}$ of about 1.5, however, pronounced deviations from the PS results emerge for several mesoscopic models. The He-Luo model displays the largest amplitude of spurious pressure oscillations, corresponding to its largest deviation from the rms pressure fluctuation compared to the PS method. The Zhang and Guo models behave almost identically: although the oscillation amplitude is reduced relative to the He-Luo model, it is not fully eliminated. In contrast, the Qi model provides a marked improvement. Even with a modest damping parameter $\chi = -0.3$, pressure oscillations are suppressed more effectively than in the Zhang and Guo models, while for a larger magnitude $\chi = -3.0$, the Qi model's results are in near-perfect agreement with the PS curve. This behavior is consistent across both Reynolds numbers considered, demonstrating that the Qi model can robustly eliminate spurious pressure fluctuations.

To quantify the discrepancy between the rms pressure obtained from mesoscopic simulations and the corresponding PS reference, we define the relative deviation

$$\Delta p_{\mathrm{rms}} = \left| \frac{p_{\mathrm{rms}}}{p^{PS}_{\mathrm{rms}}} - 1 \right|, \tag{69}$$

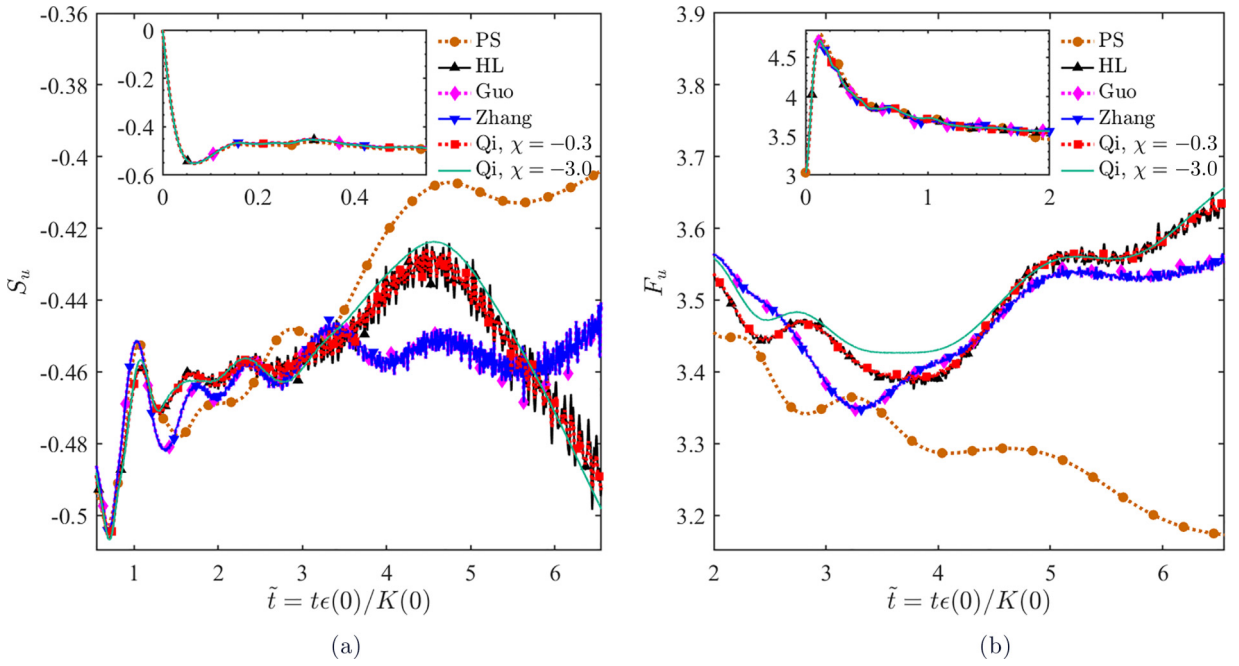



FIG. 3. Evolutions of the velocity-derivative (a) skewness $S_u$ and (b) flatness $F_u$ for $\mathrm{Re}_{\lambda,0} = 95.36$.

where $p_{\mathrm{rms}}$ is the rms pressure obtained from the mesoscopic simulations and $p_{\mathrm{rms}}^{\mathrm{PS}}$ is the corresponding reference value computed using a PS method. The relative deviations for cases 1 and 2 at selected nondimensional time $\tilde{t}$ are summarized in Table I.

Overall, as time advances, the hydrodynamic pressure associated with the flow progressively decays, while the acoustic pressure becomes increasingly prominent; consequently, the relative deviation $\Delta p_{\mathrm{rms}}$ grows with time. This trend is observed consistently for both cases across the different kinetic models. Compared with the He-Luo model, the Guo and Zhang models yield slightly smaller relative deviations, although they remain of the same order of magnitude. For the Qi model with $\chi = -0.3$, the relative deviation is further reduced and remains consistently smaller than those of the other three models. Notably, when $\chi = -3.0$ is employed, the relative deviation drops below 10% for case 2, indicating that the spurious pressure fluctuations are dramatically suppressed and the coefficient $\chi$ might be dependent on the Reynolds number.

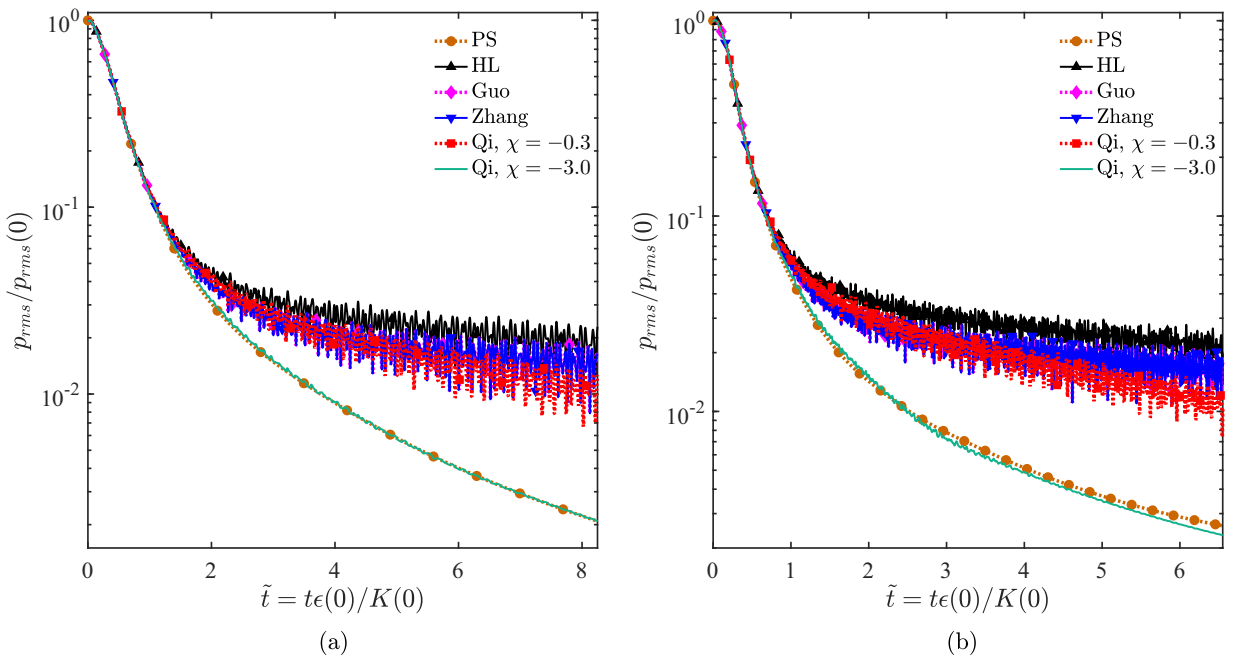



FIG. 4. Evolutions of the normalized rms pressure fluctuation $p_{\mathrm{rms}}/p_{\mathrm{rms}}(0)$ for (a) $\mathrm{Re}_{\lambda,0} = 49.02$ and (b) $\mathrm{Re}_{\lambda,0} = 95.36$.

TABLE I. Relative deviation $\Delta p_{\rm rms}$ of the rms pressure at selected times for cases 1 and 2 with different models.

| | $\Delta p_{\rm rms}$ (%) | | | | | |
|---|---|---|---|---|---|---|
| Case 1 | $\tilde{t} = 1.245$ | $\tilde{t} = 2.490$ | $\tilde{t} = 3.752$ | $\tilde{t} = 4.998$ | $\tilde{t} = 6.260$ | $\tilde{t} = 7.505$ |
| He-Luo model | 17.33 | 85.55 | 148.8 | 256.8 | 546.2 | 807.3 |
| Guo model | 4.190 | 28.61 | 139.6 | 268.3 | 360.5 | 530.4 |
| Zhang model | 4.190 | 28.61 | 139.6 | 268.3 | 360.5 | 530.4 |
| Qi model, $\chi = -0.3$ | 14.90 | 64.29 | 100.2 | 159.4 | 317.9 | 427.6 |
| Qi model, $\chi = -3.0$ | 4.095 | 3.344 | 0.9523 | 0.3428 | 0.08360 | 0.3608 |
| | $\Delta p_{\rm rms}$ (%) | | | | | |
| Case 2 | $\tilde{t} = 1.000$ | $\tilde{t} = 2.001$ | $\tilde{t} = 2.998$ | $\tilde{t} = 4.002$ | $\tilde{t} = 4.999$ | $\tilde{t} = 6.002$ |
| He-Luo model | 29.31 | 181.4 | 330.6 | 429.2 | 507.8 | 648.7 |
| Guo model | 16.18 | 124.4 | 206.9 | 340.4 | 430.1 | 375.4 |
| Zhang model | 16.18 | 124.4 | 206.9 | 340.4 | 430.1 | 375.4 |
| Qi model, $\chi = -0.3$ | 24.23 | 137.0 | 221.5 | 257.7 | 274.0 | 309.6 |
| Qi model, $\chi = -3.0$ | 4.039 | 7.802 | 6.941 | 4.956 | 5.189 | 8.308 |

Compared with the PS method, in which the velocity field is strictly divergence free, the velocity obtained by DUGKS exhibits a small but finite divergence, indicating that residual compressibility affects the small-scale dynamics. Figure 5 shows the temporal evolution of the normalized rms dilatation for the two initial Reynolds numbers considered. Because the initial velocity field is divergence free, the dilatation exhibits a drastically initial jump. Thereafter, the normalized dilatation predicted by the He-Luo, Guo, and Zhang models remains nearly constant in time: the He-Luo model yields the largest level, while the Guo and Zhang models give almost identical results at a relatively lower level. In contrast, the Qi model displays an approximately linear decay of dilatation with $\tilde{t}$, with a decay rate that increases with $|\chi|$. For sufficiently large $|\chi|$, the dilatation rapidly decreases to a level close to round-off error, indicating an effective suppression of residual compressibility effects.

Figure 6 shows the temporal evolution of the ratio between the rms dilatational velocity and the rms solenoidal velocity (hereafter referred to as the rms velocity ratio) for the different models. Overall, apart from a brief initial decrease, the velocity ratio increases with time, indicating a progressively larger contribution of dilatational motions to the turbulent field. Among the models considered, the He-Luo model yields the largest velocity ratio, followed by the Guo and Zhang models, whose results are comparable. For the Qi model,

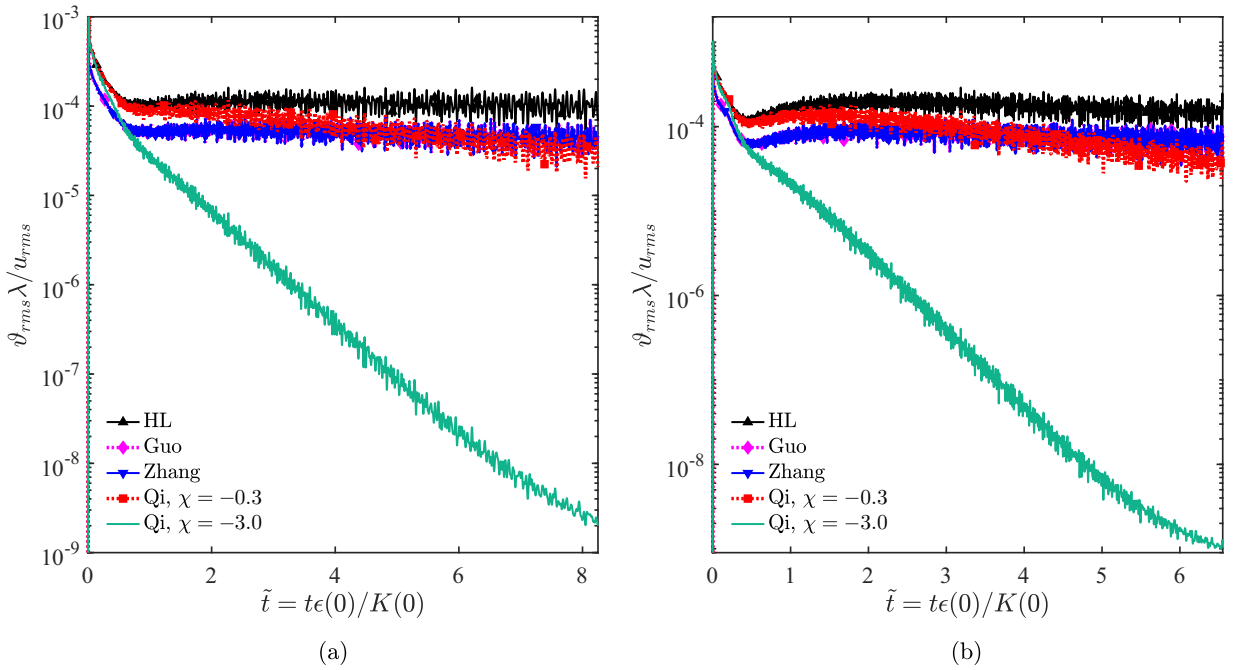



FIG. 5. Evolutions of the normalized rms dilatation $\vartheta_{\rm rms}\lambda/u_{\rm rms}$ for (a) $\mathrm{Re}_{\lambda,0} = 49.02$ and (b) $\mathrm{Re}_{\lambda,0} = 95.36$.

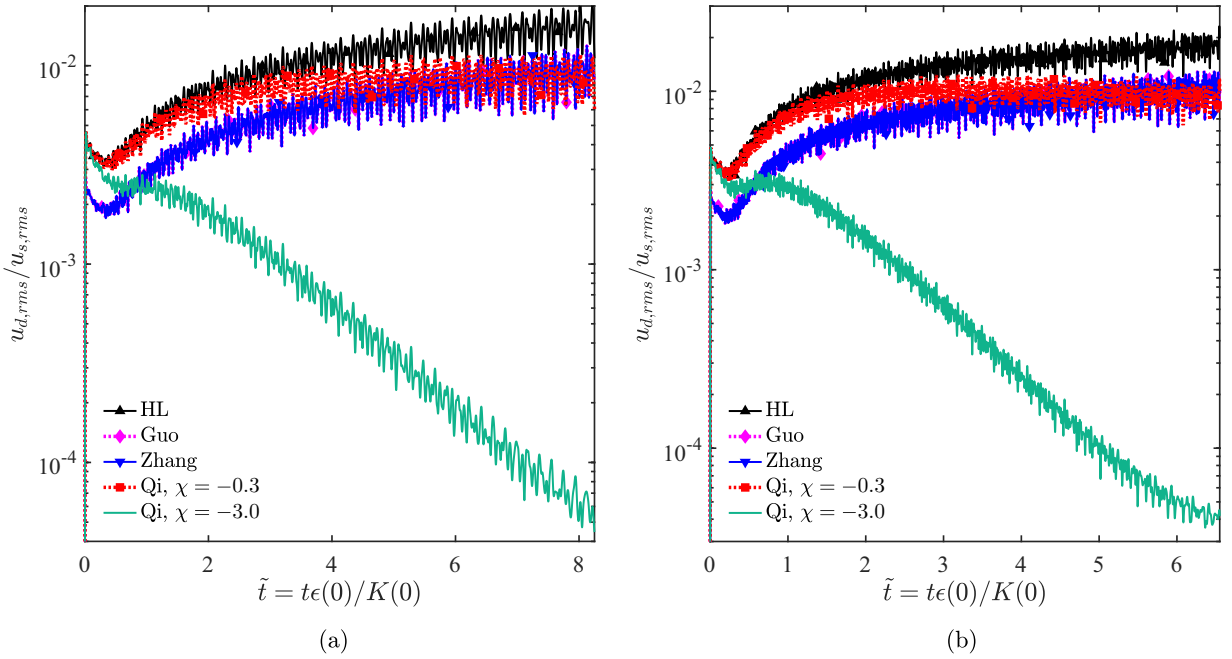



FIG. 6. Evolutions of the rms velocity ratio $u_{d,\mathrm{rms}}/u_{s,\mathrm{rms}}$ for (a) $\mathrm{Re}_{\lambda,0} = 49.02$ and (b) $\mathrm{Re}_{\lambda,0} = 95.36$.

the behavior depends sensitively on the parameter $\chi$. When $|\chi|$ is small, the velocity ratio is initially higher than that of the Guo model but subsequently decays and eventually falls below it [as shown in Fig. 6(b)]. When $|\chi|$ is sufficiently large, the velocity ratio decreases monotonically throughout the simulation. These observations indicate that the $\chi$ term effectively introduces an additional dissipation mechanism for dilatational turbulent kinetic energy, thereby efficiently suppressing compressibility-induced noise.

### C. Instantaneous flow structures

In Sec. III, we analyzed the higher-order errors introduced by different kinetic models in the recovery of viscous stresses. The analysis showed that the Guo and Zhang models exhibit identical behavior, whereas the Qi model follows the same error structure as the He-Luo model. Since all models share the same kinematic viscosity $\nu$, differences in viscous stresses are equivalent to differences in the predicted strain-rate fields. As the strain-rate fields at the two

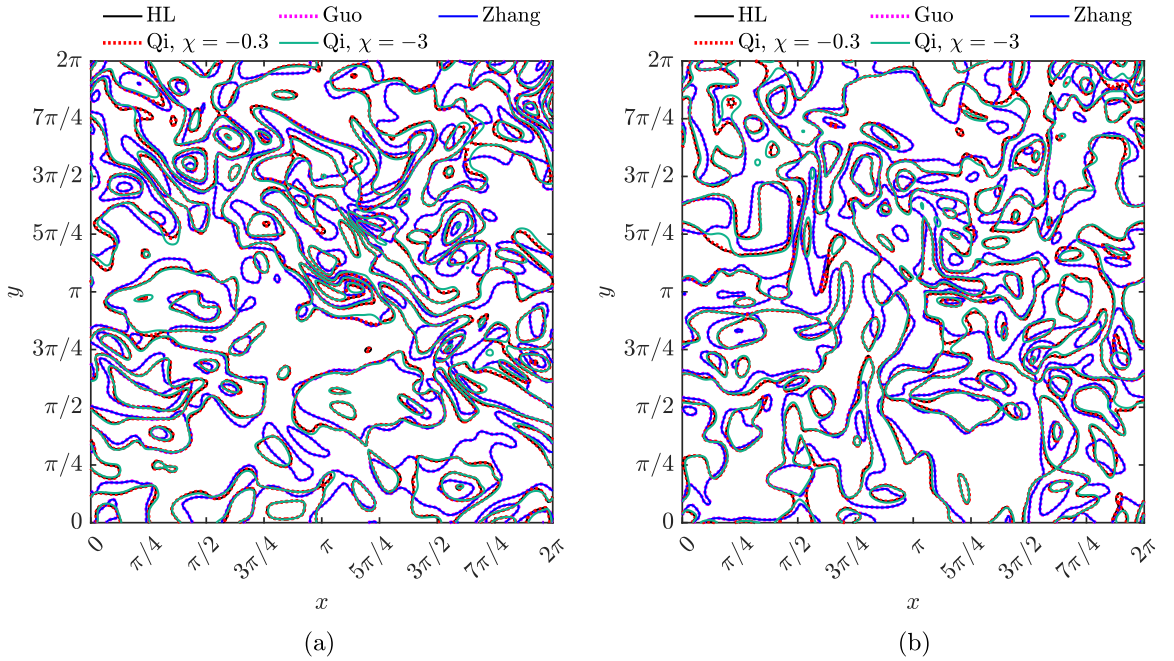



FIG. 7. Contours of the strain-rate components (a) $S_{xx}$ and (b) $S_{xy}$ on $z = \pi/2$ for $\mathrm{Re}_{\lambda,0} = 95.36$ at $\tilde{t} = 1.305$. The line styles and colors correspond to the same cases as in Fig. 6.

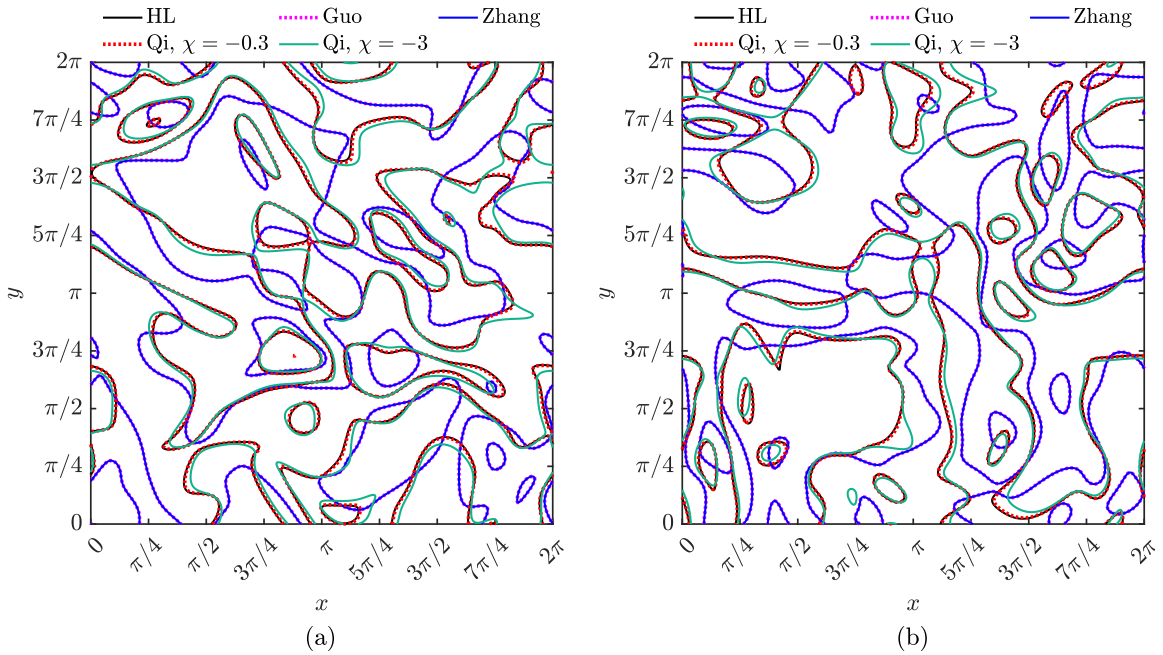



FIG. 8. Contours of the strain-rate components (a) $S_{xx}$ and (b) $S_{xy}$ on $z = \pi/2$ for $\mathrm{Re}_{\lambda,0} = 95.36$ at $\tilde{t} = 3.929$. The line colors correspond to the same cases as in Fig. 6.

Reynolds numbers exhibit qualitatively similar features, only the higher-Reynolds-number case is presented for brevity. Under isotropic conditions, we compare contours of the normal strain rate $S_{xx}$ and the shear strain rate $S_{xy}$ at two representative instants, $\tilde{t} = 1.305$ and 3.929, taken from the high-resolution $384^3$ simulation. At the earlier instant, no significant differences are observed in the skewness and flatness across different mesoscopic models. In contrast, at the later instant, apparent divergences emerge in both skewness and flatness among these models.

At $\tilde{t} = 1.305$, the skewness and the flatness are nearly identical across all models, indicating that accumulated errors have not yet led to significant divergence in small-scale structures. As shown in Fig. 7, the contours of $S_{xx}$ and $S_{xy}$ are smooth and essentially free of spurious noise and artificial compressibility. The Guo and Zhang models coincide exactly. While the overall patterns predicted by the Guo and He-Luo models are similar, discrepancies appear in local contours and the finest-scale features. The Qi model closely overlaps with the He-Luo model for small $|\chi|$; as $|\chi|$ increases, its global structure remains similar to the He-Luo model, but localized deviations emerge at small scales, with a spatial pattern distinct from that of the Guo model.

Figure 8 presents the contour fields at $\tilde{t} = 3.929$. By this stage the flow has reached a quasisteady regime: interactions among vortex tubes have weakened and the contours become noticeably sparser. The skewness and the flatness indicate that differences in the small-scale structures have already emerged. A direct comparison shows that the Guo model (which coincides with the Zhang model) differs from the He-Luo model in fine-scale features. The Qi model collapses onto the He-Luo model for small $|\chi|$; for larger $|\chi|$, it remains consistent with He-Luo at large scales but exhibits distinct deviations at small scales that are not observed in the Guo and Zhang results. Taken together with the analysis at earlier times, these contour comparisons demonstrate that the Qi model constitutes an independent kinetic model, distinct from the Guo model, while recovering the He-Luo model in the appropriate limiting case. A probable explanation for this differentiation is that the Qi model proficiently mitigates the temporal derivative of density fluctuation in the viscous stress, whereas the rest of the models fail to address the temporal derivative of density fluctuation or pressure.

## V. DISCUSSION AND CONCLUSIONS

We propose a theoretical framework for the Boltzmann model equation that enables a systematic identification of the hierarchy of macroscopic equations it can recover. Similar in spirit to the systematic analyzes of Shan *et al.* [16], the present approach is also built upon the CE analysis combined with a Hermite expansion of the equilibrium distribution while including Hilbert expansions for the Hermite coefficients. We show, however, that the framework of Shan *et al.* [16] is not readily compatible with several practically important extensions of Boltzmann model equations, such as the lattice kinetic scheme [19] and inverse-designed frameworks [24]. The underlying reason is that their Hermite expansion implicitly assumes all coefficients to be of the same Knudsen number (or relaxation time) order, which is inconsistent with the multiscale asymptotic structure inherent in the CE analysis.

To resolve this inconsistency, we further introduce a Hilbert expansion of the Hermite coefficients of the equilibrium distribution, expressing them as asymptotic series in the relaxation time. Within this extended framework, the Boltzmann model equation admits a richer kinetic hierarchy, in which different Hilbert orders correspond to distinct macroscopic evolution equations. The proposed approach not only unifies the derivation of existing models but also provides a systematic theoretical basis for the construction of

broader and more flexible mesoscopic models of complex flows.

To demonstrate the applicability of the proposed framework to Boltzmann model equations, we first formulate a general class of kinetic models for incompressible flows. Within this setting, four representative models from the literature, the athermal model [29], the He-Luo model [30], the Guo model [31], and the Zhang model [32], are systematically analyzed, together with the developed Qi model. The analysis reveals that, among existing models, the He-Luo model inevitably generates spurious pressure oscillations induced by artificial compressibility, which cannot be eliminated. Although the Guo and Zhang models recover identical macroscopic equations, they do not strictly enforce velocity divergence free and likewise lack an effective mechanism to suppress pressure oscillations. Moreover, the He-Luo and Guo models differ in the higher-order error terms associated with the recovered viscous stress. We recall that all these models are weakly compressible at the hydrodynamic level: "incompressible" refers to the low-Mach-number macroscopic regime they are designed to recover, and the Qi model suppresses the associated spurious oscillations asymptotically rather than eliminating compressibility in a strict sense.

The proposed Qi model introduces an oscillation-suppression term into the Hilbert coefficients of the equilibrium distribution, leading to a macroscopic continuity equation that combines features of artificial compressibility [33] and penalty [40] methods. This modification enables effective suppression of spurious pressure oscillations without introducing additional auxiliary variables beyond density fluctuation and velocity. The higher-order errors in the viscous stress remain identical to those of the He-Luo model, and the Qi model degenerates to the He-Luo formulation as the suppression term vanishes.

Simulations of decaying turbulence further confirm that the He-Luo, Guo, and Zhang models fail to control spurious pressure oscillations, whereas the Qi model attenuates them even for small suppression parameters and completely eliminates them for moderate values. In addition, the Qi model mitigates higher-order errors associated with the temporal derivative of density fluctuation in the viscous stress, leading to observable effects on the small-scale structure of the instantaneous strain-rate field.

## ACKNOWLEDGMENTS

This work has been supported by Science Foundation for Young Scientists of State Key Laboratory of High Temperature Gas Dynamics (Grant No. 2025QN16), Chinese Academy of Sciences Project for Young Scientists in Basic Research (Grant No. YSBR107), Strategic Priority Research Program of Chinese Academy of Sciences (Grant No. XDB0620403), the National Natural Science Foundation of China (NSFC Grants No. T2250710183, No. U2241269, No. 12302381, and No. 12572340), NSFC Excellence Research Group Program for "Multiscale Problems in Nonlinear Mechanics" (Grant No. 12588201), Beijing Natural Science Foundation (Grant No. L252039), Department of Science and Technology of Guangdong Province (Grant No. 2023B1212060001), and Guangdong-Hong Kong-Macao Joint Laboratory for Data-Driven Fluid Mechanics and Engineering Applications (Grant No. 2020B1212030001). Computing resources are provided by the Center for Computational Science and Engineering of Southern University of Science and Technology.

## DATA AVAILABILITY

The data that support the findings of this article are not publicly available. The data are available from the authors upon reasonable request.

## APPENDIX A: DERIVATION DETAILS OF THE MAJOR EQUATIONS IN SEC. II

This appendix provides the derivations of Eqs. (10), (12), (13), and (15)–(18) presented in Sec. II.

To obtain Eq. (10), one needs to evaluate the derivative of the weight function multiplied by Hermite polynomials, as well as the product of the particle velocity $\boldsymbol{\xi}$ with Hermite polynomials. Using properties of multidimensional Hermite functions [8], the following identities hold:

$$c_s\nabla_{\xi_i}\left[w(\xi,c_s)\mathcal{H}^{(n)}_{i_1\cdots i_n}\right]=-w(\xi,c_s)\mathcal{H}^{(n+1)}_{ii_1\cdots i_n}, \tag{A1}$$

$$\frac{\xi_i}{c_s}\mathcal{H}^{(n+1)}_{i_1\cdots i_{n+1}}=\mathcal{H}^{(n+2)}_{ii_1\cdots i_{n+1}}+\sum_{k=1}^{n+1}\delta_{ii_k}\mathcal{H}^{(n)}_{i_1\cdots i_{k-1}i_{k+1}\cdots i_{n+1}}. \tag{A2}$$

For clarity of presentation, the Hermite expansion of the equilibrium distribution in Eq. (10) is first considered without truncation. The generalized CE expansion of the distribution with an infinite-order Hermite equilibrium can then be written in the form

$$\begin{aligned}
f^{(+\infty)}&=\sum_{r=0}^{+\infty}\frac{1}{r!}\left[1-\tau\frac{D}{Dt}+O(\tau^2)\right]w(\xi,c_s)\\
&\quad\times\left[a_i^{(r,0)}+\tau a_i^{(r,1)}+O(\tau^2)\right]\mathcal{H}_i^{(r)}\\
&=w\sum_{r=0}^{+\infty}\frac{1}{r!}\left[a_i^{(r,0)}+\tau\left(a_i^{(r,1)}-\frac{\partial}{\partial t}a_i^{(r,0)}\right)\right]\mathcal{H}_i^{(r)}\\
&\quad-\tau\sum_{r=0}^{+\infty}\frac{1}{r!}(\boldsymbol{\xi}\cdot\nabla+\boldsymbol{b}\cdot\nabla_{\xi})\left[wa_i^{(r,0)}\mathcal{H}_i^{(r)}\right]+O(\tau^2)\\
&=w\sum_{r=0}^{+\infty}\frac{1}{r!}\left[a_{i_1\cdots i_r}^{(r,0)}+\tau\left(a_{i_1\cdots i_r}^{(r,1)}-\frac{\partial}{\partial t}a_{i_1\cdots i_r}^{(r,0)}\right)\right]\mathcal{H}_{i_1\cdots i_r}^{(r)}\\
&\quad-\tau w\sum_{r=0}^{+\infty}\frac{1}{r!}\left[c_s\nabla_i a_{i_1\cdots i_r}^{(r,0)}\frac{\xi_i}{c_s}\mathcal{H}_{i_1\cdots i_r}^{(r)}-\frac{b_i}{c_s}a_{i_1\cdots i_r}^{(r,0)}\mathcal{H}_{ii_1\cdots i_r}^{(r+1)}\right]\\
&\quad+O(\tau^2)\\
&=w\begin{Bmatrix}\sum_{r=0}^{+\infty}\frac{1}{r!}\left[a_{i_1\cdots i_r}^{(r,0)}+\tau\left(a_{i_1\cdots i_r}^{(r,1)}-\frac{\partial}{\partial t}a_{i_1\cdots i_r}^{(r,0)}\right)\right]\mathcal{H}_{i_1\cdots i_r}^{(r)}\\+\tau\sum_{r=0}^{+\infty}\frac{1}{r!}\left(\frac{b_i}{c_s}-c_s\nabla_i\right)a_{i_1\cdots i_r}^{(r,0)}\mathcal{H}_{ii_1\cdots i_r}^{(r+1)}\\-\tau\sum_{r=1}^{+\infty}\frac{1}{(r-1)!}c_s\nabla_{\xi_i}a_{i_1\cdots i_r}^{(r,0)}\mathcal{H}_{i_2\cdots i_r}^{(r-1)}+O(\tau^2)\end{Bmatrix},
\end{aligned} \tag{A3}$$

where the simplification follows directly from the identities Eqs. (A1) and (A2). The expression presented in Eq. (10)

is subsequently obtained by truncating the generalized CE expansion Eq. (A3) at order $R$.

Substituting the generalized CE expansion Eq. (10) into the conservation relations at the NS level, given by Eq. (11), requires that all terms except the leading one yield vanishing contributions to the moments of the conserved variables $\boldsymbol{\psi}$ at $\boldsymbol{O}(\tau)$. Owing to the orthogonality of Hermite polynomials, these moment integrals reduce to the Euler-level macroscopic equations Eqs. (12) and (13):

$$\int \left[\frac{\partial}{\partial t}a^{(0,0)} + c_s\nabla_i a_i^{(1,0)} - a^{(0,1)}\right]\mathcal{H}^{(0)}d\boldsymbol{\xi} = \frac{\partial}{\partial t}a^{(0,0)} + c_s\nabla_i a_i^{(1,0)} - a^{(0,1)} = O(\tau), \tag{A4}$$

$$\int \left[\frac{\partial}{\partial t}a_j^{(1,0)} + c_s\nabla_k a_{jk}^{(2,0)} + \left(c_s\nabla_j - \frac{b_j}{c_s}\right)a^{(0,0)} - a_j^{(1,1)}\right]\xi_i\mathcal{H}_j^{(1)}d\boldsymbol{\xi} = c_s\frac{\partial}{\partial t}a_i^{(1,0)} + c_s^2\nabla_k a_{ik}^{(2,0)} + \left(c_s^2\nabla_i - b_i\right)a^{(0,0)} - c_s a_i^{(1,1)} = O(\tau). \tag{A5}$$

Taking the time derivative of Eq. (A4) and subtracting the divergence of Eq. (A5) eliminates the intermediate terms and yields a wave equation for the zeroth-order Hermite coefficient $a^{(0,0)}$,

$$\frac{\partial^2}{\partial t^2}a^{(0,0)} - \frac{\partial}{\partial t}a^{(0,1)} = c_s^2\nabla^2 a^{(0,0)} - \nabla_i\left(c_s a_i^{(1,1)} + b_i a^{(0,0)}\right) + c_s^2\nabla_i\nabla_k a_{ik}^{(2,0)} + O(\tau), \tag{A6}$$

which corresponds to Eq. (15).

The recovered macroscopic equations can also be derived by taking velocity moments of the Boltzmann model equation with respect to the conserved variables, together with the conservation relation Eq. (8). This leads to

$$\int\left(\frac{Df}{Dt} + \frac{f - f^{\mathrm{eq}}}{\tau}\right)d\boldsymbol{\xi} = \frac{\partial}{\partial t}a^{(0,0)} + c_s\nabla_i a_i^{(1,0)} + \int\frac{f^{\mathrm{eq},(\infty,0)} - f^{\mathrm{eq}}}{\tau}d\boldsymbol{\xi} = 0, \tag{A7}$$

$$\int\left(\frac{Df}{Dt} + \frac{f - f^{\mathrm{eq}}}{\tau}\right)\xi_i d\boldsymbol{\xi} = c_s\frac{\partial}{\partial t}a_i^{(1,0)} + c_s^2\nabla_i\left(a^{(0,0)}I_{ij} + a_{ij}^{(2,0)}\right) - \nabla_i\sigma_{ij} - b_i a^{(0,0)} + \int\frac{f^{\mathrm{eq},(\infty,0)} - f^{\mathrm{eq}}}{\tau}\xi_i d\boldsymbol{\xi} = 0, \tag{A8}$$

$$\sigma_{ij} = \int\xi_i\xi_j[f^{\mathrm{eq},(\infty,0)} - f]d\boldsymbol{\xi} = \int c_i c_j[f^{\mathrm{eq},(\infty,0)} - f]d\boldsymbol{\xi}. \tag{A9}$$

To recover the Euler equations, the distribution function is approximated by the zeroth-order CE expansion, $f = f^{\mathrm{eq},(\infty,0)} + O(\tau)$. Under this approximation, the velocity moments appearing in Eqs. (A7)–(A9) reduce to

$$\int\frac{f^{\mathrm{eq},(\infty,0)} - f^{\mathrm{eq}}}{\tau}d\boldsymbol{\xi} = -a^{(0,1)} + O(\tau), \tag{A10}$$

$$\int\frac{f^{\mathrm{eq},(\infty,0)} - f^{\mathrm{eq}}}{\tau}\xi_i d\boldsymbol{\xi} = -c_s a_i^{(1,1)} + O(\tau), \tag{A11}$$

$$\sigma_{ij} = \int c_i c_j\left[f^{\mathrm{eq},(\infty,0)} - f\right]d\boldsymbol{\xi} = O(\tau). \tag{A12}$$

Substituting these expressions into Eqs. (A7) and (A8) yields results identical to Eqs. (A4) and (A5), and hence the Euler equations Eqs. (12) and (13).

To recover the NS-level macroscopic equations Eqs. (16) and (17), a higher-order expansion of $f$ is required. Retaining the first-order CE expansion,

$$f = f^{\mathrm{eq},(\infty,1)} - \tau\frac{D}{Dt}f^{\mathrm{eq},(\infty,0)} + O(\tau^2), \tag{A13}$$

and substituting it into the above velocity moments gives

$$\int\frac{f^{\mathrm{eq},(\infty,0)} - f^{\mathrm{eq}}}{\tau}d\boldsymbol{\xi} = -a^{(0,1)} - \tau a^{(0,2)} + O(\tau^2), \tag{A14}$$

$$\int\frac{f^{\mathrm{eq},(\infty,0)} - f^{\mathrm{eq}}}{\tau}\xi_i d\boldsymbol{\xi} = -c_s a_i^{(1,1)} - c_s\tau a_i^{(1,2)} + O(\tau^2), \tag{A15}$$

$$\sigma_{ij} = \int\xi_i\xi_j\left[\tau\frac{D}{Dt}f^{\mathrm{eq},(\infty,0)} + f^{\mathrm{eq},(\infty,0)} - f^{\mathrm{eq},(\infty,1)}\right]d\boldsymbol{\xi} + O(\tau^2) = \tau\begin{Bmatrix}\partial\left(c_s^2 a_{ij}^{(2,0)} - I_{ij}a^{(0,0)}\right)/\partial t - c_s\left(b_i a_j^{(1,0)} + b_j a_i^{(1,0)}\right) - I_{ij}a^{(0,1)} \\ -c_s^2 a_{ij}^{(2,1)} + \nabla_k\left[c_s^3 a_{ijk}^{(3,0)} + c_s\left(I_{ij}a_k^{(1,0)} + I_{ik}a_j^{(1,0)} + I_{jk}a_i^{(1,0)}\right)\right]\end{Bmatrix} + O(\tau^2)$$

$$= \tau\begin{Bmatrix}c_s^2\partial a_{ij}^{(2,0)}/\partial t - c_s\left(b_i a_j^{(1,0)} + b_j a_i^{(1,0)}\right) - c_s^2 a_{ij}^{(2,1)} \\ +\nabla_k\left[c_s^3 a_{ijk}^{(3,0)} + c_s\left(I_{ik}a_j^{(1,0)} + I_{jk}a_i^{(1,0)}\right)\right]\end{Bmatrix} + O(\tau^2). \tag{A16}$$

In simplifying Eq. (A16), the Euler-level continuity equation Eq. (12) has been used; the resulting expression coincides with the viscous stress tensor given in Eq. (18). Finally, substituting Eqs. (A14)–(A16) into the velocity-moment

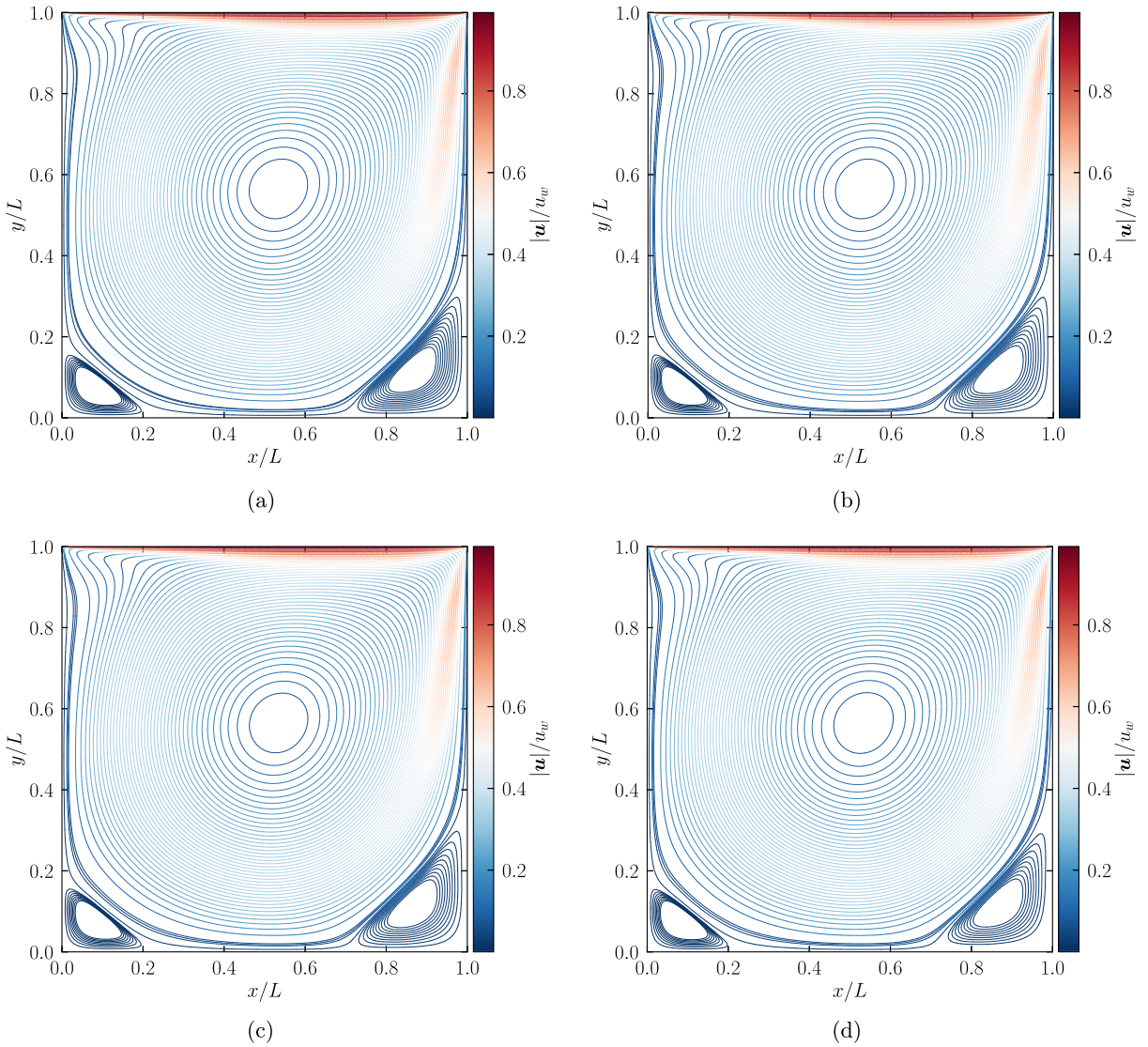



FIG. 9. Streamlines of the two-dimensional lid-driven cavity flow at Re = 1000, colored by the normalized velocity magnitude: (a) He-Luo model, (b) Guo model, (c) Zhang model, and (d) Qi model with $\chi = -3$.

equations Eqs. (A7) and (A8) yields the NS-level macroscopic equations Eqs. (16) and (17). Here, based on the velocity-moment formulation Eq. (14) of the Boltzmann model equation and the conservation relations Eq. (8), we systematically derive the Euler equations Eqs. (12) and (13), the NS equations Eqs. (16) and (17), and the associated viscous stress Eq. (18) at the NS level.

## APPENDIX B: THE BOUNDARY CONDITION FOR THE KINETIC MODELS IN INCOMPRESSIBLE FLOWS

Appendix B derives an on-wall bounce-back boundary condition for the distribution function, tailored to the incompressible flows in Sec. III. The construction is based on the velocity moment constraints imposed by the conservation relations Eq. (8) and the viscous stress Eq. (24). Specifically, the deviation of the distribution function from the zeroth-order equilibrium $f^{\mathrm{eq},(2,0)}$ satisfies

$$\int [f^{\mathrm{eq},(2,0)} - f] d\boldsymbol{\xi} = O(\tau^2),$$

$$\int \boldsymbol{\xi} [f^{\mathrm{eq},(2,0)} - f] d\boldsymbol{\xi} = \boldsymbol{O}(\tau^2), \tag{B1a}$$

$$\int \boldsymbol{cc} [f^{\mathrm{eq},(2,0)} - f] d\boldsymbol{\xi} = \boldsymbol{\sigma}. \tag{B1b}$$

These constraints lead to a Hermite expansion for the deviation of the distribution function from the zeroth-order equilibrium,

$$f^{\mathrm{eq},(2,0)} - f = \frac{w(\xi, c_s)}{2c_s^2} \left( \frac{\boldsymbol{\xi} \cdot \boldsymbol{\sigma} \cdot \boldsymbol{\xi}}{c_s^2} - \sigma_{ii} \right), \tag{B2}$$

which is identical in form to the nonequilibrium distribution obtained by Krüger *et al.* [50] for incompressible flows. Consequently, the distribution function in the incompressible

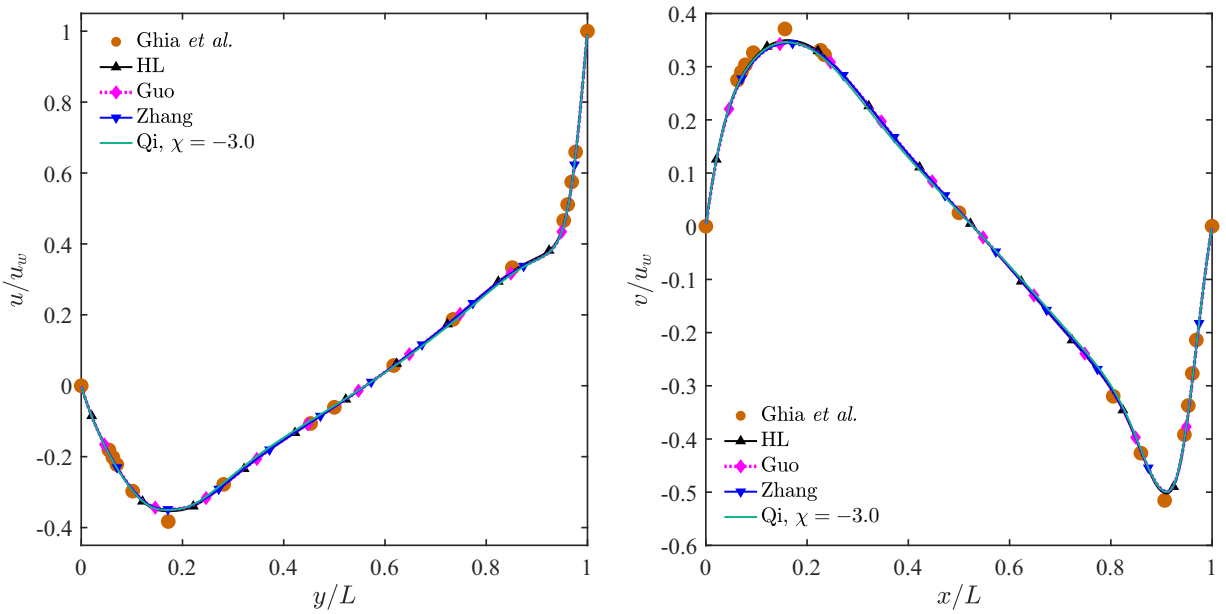



FIG. 10. Velocity profiles for the two-dimensional lid-driven cavity flow at Re = 1000: (a) normalized horizontal velocity $u/u_w$ along the vertical centerline $x/L = 0.5$ and (b) normalized vertical velocity $v/u_w$ along the horizontal centerline $y/L = 0.5$.

flows can be written as

$$f = w(\xi, c_s)\left[\sum_{r=0}^{2} \frac{1}{r!} a^{(r,0)}_{i_1\cdots i_r} \mathcal{H}^{(r)}_{i_1\cdots i_r} + \frac{1}{2c_s^2}\left(\sigma_{ii} - \frac{\boldsymbol{\xi}\cdot\boldsymbol{\sigma}\cdot\boldsymbol{\xi}}{RT_0}\right)\right]. \tag{B3}$$

From this expression, the distribution function, its equilibrium, and the associated forcing term along a given discrete velocity direction are related to those along the corresponding bounce-back direction by

$$f(\boldsymbol{\xi}) - f(-\boldsymbol{\xi}) = 2w(\xi, c_s)\boldsymbol{a}^{(1,0)} \cdot \boldsymbol{\mathcal{H}}^{(1)}(\boldsymbol{\xi}), \tag{B4a}$$

$$f^{\mathrm{eq},(2,1)}(\boldsymbol{\xi}) - f^{\mathrm{eq},(2,1)}(-\boldsymbol{\xi}) = 2w(\xi, c_s)\left[a_i^{(1,0)} + \tau a_i^{(1,1)} + \tau^2 a_i^{(1,2)}\right]H_i^{(1)}(\boldsymbol{\xi}), \tag{B4b}$$

$$(\boldsymbol{b}\cdot\nabla_{\boldsymbol{\xi}} f)^{(2)}(\boldsymbol{\xi}) - (\boldsymbol{b}\cdot\nabla_{\boldsymbol{\xi}} f)^{(2)}(-\boldsymbol{\xi}) = 2w(\xi, c_s)\boldsymbol{B}^{(1)} \cdot \boldsymbol{\mathcal{H}}^{(1)}(\boldsymbol{\xi}). \tag{B4c}$$

For the classical DUGKS [14,51], the half-time-step distribution at a cell interface is given by

$$\overline{f} = \frac{2\tau + \delta t}{2\tau} f - \frac{\delta t}{2\tau} f^{\mathrm{eq},(2,1)} + \frac{\delta t}{2}(\boldsymbol{b}\cdot\nabla_{\boldsymbol{\xi}} f)^{(2)}, \tag{B5}$$

where $\delta t$ is the half time step. Combining this expression with the bounce-back symmetry yields a unified on-wall bounce-back boundary condition applicable to the He-Luo, Guo, Zhang, and Qi models,

$$\overline{f}(\boldsymbol{\xi}) - \overline{f}(-\boldsymbol{\xi}) = 2w(\xi, c_s)\rho_0\left(\boldsymbol{u} - \frac{\delta t}{2}\boldsymbol{b}\right)\cdot\frac{\boldsymbol{\xi}}{c_s^2}, \tag{B6}$$

where the macroscopic velocity $\boldsymbol{u}$ is prescribed by the wall motion. Numerical results for the two-dimensional lid-driven cavity flow obtained using this boundary condition are presented in Appendix E.

## APPENDIX C: A BRIEF DESCRIPTION OF THE DISCRETE UNIFIED GAS KINETIC SCHEME

Here we briefly describe the discrete unified gas kinetic scheme [14,51] used for all the simulations in this work; further implementation details can be found in Qi *et al.* [43,44]. DUGKS [14] is a finite-volume scheme in which the computational domain is divided into many connected cells $V_i$ centered at $\boldsymbol{x}_i$. Employing the midpoint rule for the convective term and the trapezoidal rule for the collision term, Eq. (1) is integrated over the cell $V_i$ from $t_n$ to $t_{n+1} = t_n + \Delta t$, which yields

$$\left(\widetilde{f}\right)_i^{n+1} = \left(\widetilde{f^+}\right)_i^n - \frac{\Delta t}{|V_i|}\oint_{\partial V_i} (\boldsymbol{\xi}\cdot\boldsymbol{n}) f(\boldsymbol{x}_b, t_{n+1/2})\, dS, \tag{C1}$$

where the subscript $i$ and the superscript $n$ denote the cell-averaged value over the cell $V_i$ at time $t_n$, and $f(\boldsymbol{x}_b, t_{n+1/2})$ is the distribution function at the cell interface center $\boldsymbol{x}_b$ at the half time step $t_{n+1/2} = t_n + \delta t$ with $\delta t = \Delta t/2$. Two linear transformations,

$$\widetilde{f} = \frac{2\tau + \Delta t}{2\tau} f - \frac{\Delta t}{2\tau} f^{\mathrm{eq}}, \quad \widetilde{f^+} = \frac{2\tau - \Delta t}{2\tau} f + \frac{\Delta t}{2\tau} f^{\mathrm{eq}}, \tag{C2}$$

are introduced to convert the implicit scheme into an explicit one. The flux distribution $f(\boldsymbol{x}_b, t_{n+1/2})$ is evaluated by integrating Eq. (1) along the characteristic line using the trapezoidal rule. Introducing another two auxiliary distribution functions,

$$\overline{f} = \frac{2\tau + \delta t}{2\tau} f - \frac{\delta t}{2\tau} f^{\mathrm{eq}}, \quad \overline{f^+} = \frac{2\tau - \delta t}{2\tau} f + \frac{\delta t}{2\tau} f^{\mathrm{eq}}, \tag{C3}$$

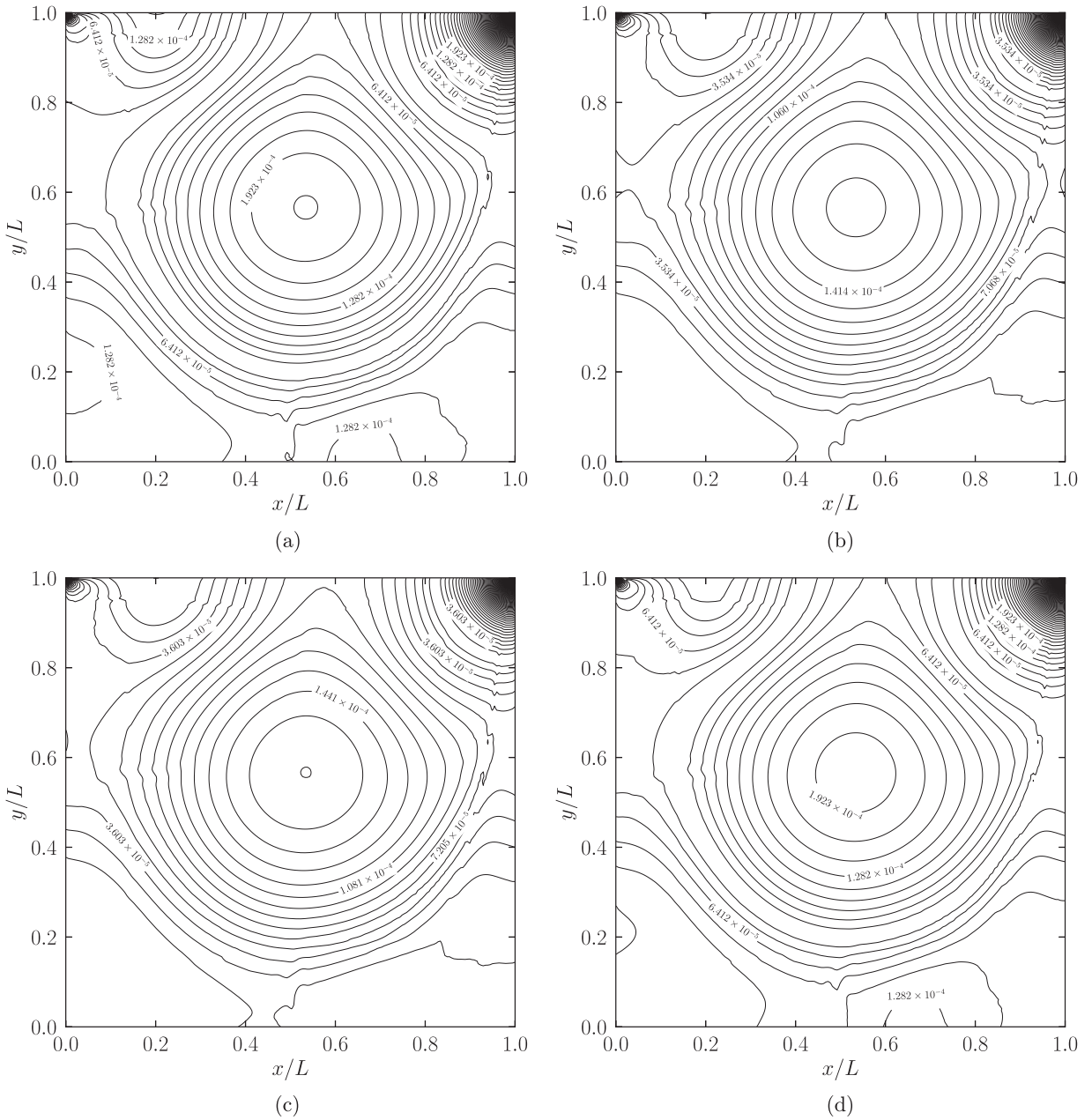



FIG. 11. Pressure contours of the two-dimensional lid-driven cavity flow at Re = 1000: (a) He-Luo model, (b) Guo model, (c) Zhang model, and (d) Qi model with $\chi = -3$.

the interface distribution is obtained explicitly as

$$\overline{f}(\boldsymbol{x}_b, t_n + \delta t) = \overline{f}^{+}(\boldsymbol{x}_b - \boldsymbol{\xi}\delta t, t_n) \approx \overline{f}^{+}(\boldsymbol{x}_i, t_n) + (\boldsymbol{x}_b - \boldsymbol{x}_i - \boldsymbol{\xi}\delta t) \cdot \nabla \overline{f}^{+}(\boldsymbol{x}_i, t_n), \quad \text{(C4)}$$

i.e., $\overline{f}^{+}(\boldsymbol{x}_b - \boldsymbol{\xi}\delta t, t_n)$ is Taylor expanded about the cell center, where the cell-center value $\overline{f}^{+}(\boldsymbol{x}_i, t_n)$ equals the cell-averaged value and can be expressed in terms of $(\widetilde{f})_i^n$ and the equilibrium distribution, and the gradient $\nabla \overline{f}^{+}(\boldsymbol{x}_i, t_n)$ is computed from the cell-averaged values with the sixth-order targeted essentially nonoscillatory scheme [52]. Because the particle transport and collision are coupled within each time step, the DUGKS is second-order accurate in space and time and asymptotic preserving: in the continuum limit the time step is restricted only by the Courant-Friedrichs-Lewy condition based on the particle velocities, rather than by the relaxation time. Combined with the off-lattice velocity sets of Appendix D, these properties make the DUGKS well suited to the mesoscopic simulations of the present study.

## APPENDIX D: D2Q9A5 AND D3V13A5 VELOCITY SETS

The D2Q9A5 discrete velocity set [16] is employed in the DUGKS for two-dimensional simulations. The D3V13A5 discrete velocity set [16,45] is used for three-dimensional simulations. Both velocity sets are listed in Table II.

TABLE II. The velocity sets D2Q9A5 and D3V13A5. The subscript "$p$" means the parity of the permutation is strictly kept.

| Model | Group | Number | Abscissa $\boldsymbol{\xi}_\alpha/c_s$ | Weight $w_\alpha$ |
|---|---|---|---|---|
| D2Q9A5 | 1 | 1 | $(0, 0)$ | 4/9 |
| $r^2 = 3$ | 2 | 4 | $(r, 0)$ | 1/9 |
| | 3 | 4 | $(r, r)$ | 1/36 |
| D3V13A5 | 1 | 1 | $(0, 0, 0)$ | 2/5 |
| $r^2 = (5+\sqrt{5})/2$, $s^2 = (5-\sqrt{5})/2$ | 2 | 12 | $(r, s, 0)_p$ | 1/20 |

## APPENDIX E: THE SIMULATIONS FOR THE TWO-DIMENSIONAL LID-DRIVEN CAVITY FLOW

Appendix E presents numerical results for the two-dimensional lid-driven cavity flow, a classical benchmark problem for assessing numerical methods and evaluating incompressible-flow solvers. The computational domain is the square $[0, L] \times [0, L]$, where $L$ denotes the cavity length. The velocity boundary conditions are prescribed as $\boldsymbol{u} = (u_w, 0)$ at the moving lid $y = L$, while no-slip conditions, $\boldsymbol{u} = \boldsymbol{0}$, are imposed on the remaining three walls. The Reynolds number is defined as $\mathrm{Re} = u_w L/\nu$. Owing to the velocity discontinuities at the two upper corners $(0, L)$ and $(L, L)$, this problem exhibits singularities at which both pressure and vorticity become unbounded, making an accurate assessment of numerical solutions particularly challenging.

Simulations are performed using the He-Luo [30], Guo [31], Zhang [32], and Qi models (with $\chi = -3$). All computations are based on the DUGKS framework [14], with the velocity boundary conditions translated into the distribution-function boundary treatment described in Appendix B and the D2Q9A5 velocity set for the particle velocity space shown in Appendix D. Spatial discretization employs a nonuniform mesh to enhance resolution near the walls, thereby improving the prediction of near-boundary flow features. A $128 \times 128$ grid is used, with mesh stretching following the formulation given in Eq. (46) of Guo *et al.* [14]. Steady state is deemed to be reached when the relative residual satisfies

$$\frac{\sum_i |u(\boldsymbol{x}_i, t_n + \Delta t) - u(\boldsymbol{x}_i, t_n)|}{\Delta t \sum_i u(\boldsymbol{x}_i, t_n)} < 10^{-8},$$
$$\frac{\sum_i |v(\boldsymbol{x}_i, t_n + \Delta t) - v(\boldsymbol{x}_i, t_n)|}{\Delta t \sum_i v(\boldsymbol{x}_i, t_n)} < 10^{-8}. \quad \text{(E1)}$$

We present simulation results at a Reynolds number of $\mathrm{Re} = 1000$. The streamlines colored by the normalized velocity magnitude are shown in Fig. 9. At this Reynolds number, the flow is characterized by a primary vortex occupying the cavity core and two secondary vortices near the lower corners. All four models accurately capture this canonical flow topology.

Velocity profiles of the horizontal velocity component $u$ along the vertical centerline $x/L = 0.5$ and of the vertical component $v$ along the horizontal centerline $y/L = 0.5$ are plotted in Fig. 10. Reference data are taken from the classical results of Ghia *et al.* [53], obtained using a multigrid vorticity-stream function formulation. The excellent agreement between the present results and the reference data for all four models demonstrates that the Qi model remains reliable for wall-bounded flow simulations.

Finally, pressure contours for the four models at $\mathrm{Re} = 1000$ are shown in Fig. 11. The presence of velocity singularities at the upper corners strongly influences the pressure field, leading to nonsmooth distortions of the contours that are intrinsic to the problem rather than to the numerical method or model employed. All four models exhibit pressure contour distortions near the upper-left and upper-right corners. Notably, the Qi model with $\chi = -3$ shows a comparatively weaker distortion, and in the lower half of the cavity ($0 < y/L < 0.5$) its pressure contours are visibly smoother than those obtained with the other models, consistent with the strong damping of spurious acoustic pressure observed in the decaying-turbulence simulations of Sec. IV. This qualitative comparison suggests that the Qi model provides a degree of suppression of pressure noise introduced by the corner singularities.


[1] S. Chapman and T. G. Cowling, *The Mathematical Theory of Non-Uniform Gases*, 3rd ed. (Cambridge University, New York, 1939).

[2] H. Grad, On the kinetic theory of rarefied gases, Commun. Pure Appl. Math. **2**, 331 (1949).

[3] H. Grad, Principles of the kinetic theory of gases, in *Thermodynamik der Gase/Thermodynamics of Gases*, edited by S. Flügge (Springer-Verlag, Berlin, 1958), pp. 205–294.

[4] T. Ohwada, and K. Xu, The kinetic scheme for the full-Burnett equations, J. Comput. Phys. **201**, 315 (2004).

[5] D. Burnett, The distribution of molecular velocities and the mean motion in a non-uniform gas, Proc. Lond. Math. Soc. **s2-40**, 382 (1936).

[6] E. Ikenberry and C. Truesdell, On the pressures and the flux of energy in a gas according to Maxwell's kinetic theory, I, J. Ration. Mech. Anal. **5**, 1 (1956).

[7] H. Struchtrup, Some remarks on the equations of Burnett and Grad, in *Transport in Transition Regimes*, edited by N. Ben Abdallah, Irene M. Gamba, C. Ringhofer, A. Arnold, R. T. Glassey, P. Degond, and C. David Levermore (Springer, New York, 2004), pp. 265–276.

[8] H. Grad, Note on $N$-dimensional Hermite polynomials, Commun. Pure Appl. Math. **2**, 325 (1949).

[9] A. V. Bobylëv, On the Chapman-Enskog and Grad methods for solving the Boltzmann equation, Dokl. Akad. Nauk SSSR **262**, 71 (1982).

[10] L. Saint-Raymond, A mathematical PDE perspective on the Chapman-Enskog expansion, Bull. Amer. Math. Soc. **51**, 247 (2014).

[11] M. Torrilhon, Modeling nonequilibrium gas flow based on moment equations, Annu. Rev. Fluid Mech. **48**, 429 (2016).

[12] C. K. Aidun and J. R. Clausen, Lattice-Boltzmann method for complex flows, Annu. Rev. Fluid Mech. **42**, 439 (2010).

[13] S. Chen and G. D. Doolen, Lattice Boltzmann method for fluid flows, Annu. Rev. Fluid Mech. **30**, 329 (1998).

[14] Z. Guo, K. Xu and R. Wang, Discrete unified gas kinetic scheme for all Knudsen number flows: Low-speed isothermal case, Phys. Rev. E **88**, 033305 (2013).

[15] C. Shu, Y. Wang, L. M. Yang, and J. Wu, Lattice Boltzmann flux solver: An efficient approach for numerical simulation of fluid flows, Trans. Nanjing Univ. Aeronaut. Astronaut. **31**, 1 (2014).

[16] X. Shan, X.-F. Yuan, and H. Chen, Kinetic theory representation of hydrodynamics: A way beyond the Navier–Stokes equation, J. Fluid Mech. **550**, 413 (2006).

[17] P. L. Bhatnagar, E. P. Gross, and M. Krook, A model for collision processes in gases. I. Small amplitude processes in charged and neutral one-component systems, Phys. Rev. **94**, 511 (1954).

[18] E. M. Shakhov, Generalization of the Krook kinetic relaxation equation, Fluid Dyn. **3**, 95 (1968).

[19] T. Inamuro, A lattice kinetic scheme for incompressible viscous flows with heat transfer, Phil. Trans. R. Soc. A **360**, 477 (2002).

[20] L. Wang, J. Mi, and Z. Guo, A modified lattice Bhatnagar-Gross-Krook model for convection heat transfer in porous media, Int. J. Heat Mass Transf. **94**, 269 (2016).

[21] Y. Kataoka and T. Inamuro, Numerical simulations of the behaviour of a drop in a square pipe flow using the two-phase lattice Boltzmann method, Phil. Trans. R. Soc. A **369**, 2528 (2011).

[22] L. Wang, J. Mi, X. Meng, and Z. Guo, A localized mass-conserving lattice Boltzmann approach for non-Newtonian fluid flows, Commun. Comput. Phys. **17**, 908 (2015).

[23] M. Yoshino, Y. Hotta, T. Hirozane, and M. Endo, A numerical method for incompressible non-Newtonian fluid flows based on the lattice Boltzmann method, J. Non-Newtonian Fluid Mech. **147**, 69 (2007).

[24] T. Chen, L.-P. Wang, J. Lai, and S. Chen, Inverse design of mesoscopic models for compressible flow using the Chapman-Enskog analysis, Adv. Aerodyn. **3**, 5 (2021).

[25] L. Djenidi, Lattice-Boltzmann simulation of grid-generated turbulence, J. Fluid Mech. **552**, 13 (2006).

[26] B. Dorschner, F. Bösch, S. S. Chikatamarla, K. Boulouchos, and I. V. Karlin, Entropic multi-relaxation time lattice Boltzmann model for complex flows, J. Fluid Mech. **801**, 623 (2016).

[27] Y. Li, R. Shock, R. Zhang, and H. Chen, Numerical study of flow past an impulsively started cylinder by the lattice-Boltzmann method, J. Fluid Mech. **519**, 273 (2004).

[28] G. Silva and V. Semiao, First- and second-order forcing expansions in a lattice Boltzmann method reproducing isothermal hydrodynamics in artificial compressibility form, J. Fluid Mech. **698**, 282 (2012).

[29] Y. H Qian, D. D'Humières, and P. Lallemand, Lattice BGK models for Navier-Stokes equation, Europhys. Lett. **17**, 479 (1992).

[30] X. He and L.-S. Luo, Lattice Boltzmann model for the incompressible Navier–Stokes equation, J. Stat. Phys. **88**, 927 (1997).

[31] Z. Guo, B. Shi, and N. Wang, Lattice BGK model for incompressible Navier–Stokes equation, J. Comput. Phys. **165**, 288 (2000).

[32] L. Zhang, Z. Zeng, H. Xie, X. Tao, Y. Zhang, Y. Lu, A. Yoshikawa, and Y. Kawazoe, An alternative lattice Boltzmann model for three-dimensional incompressible flow, Comput. Math. Appl. **68**, 1107 (2014).

[33] A. J. Chorin, A numerical method for solving incompressible viscous flow problems, J. Comput. Phys. **2**, 12 (1967).

[34] T. Ohwada and P. Asinari, Artificial compressibility method revisited: Asymptotic numerical method for incompressible Navier–Stokes equations, J. Comput. Phys. **229**, 1698 (2010).

[35] T. Ohwada, P. Asinari, and D. Yabusaki, Artificial compressibility method and lattice Boltzmann method: Similarities and differences, Comput. Math. Appl. **61**, 3461 (2011).

[36] P. V. Coveney, S. Succi, D. d'Humières, I. Ginzburg, M. Krafczyk, P. Lallemand, and L.-S. Luo, Multiple–relaxation–time lattice Boltzmann models in three dimensions, Phil. Trans. R. Soc. A **360**, 437 (2002).

[37] J. R. Clausen, Entropically damped form of artificial compressibility for explicit simulation of incompressible flow, Phys. Rev. E **87**, 013309 (2013).

[38] Y. Qi, L.-P. Wang, Z. Guo, and S. Chen, Analysis and removal of spurious pressure oscillations in Boltzmann-equation-based mesoscopic simulation of incompressible turbulence. J. Fluid Mech. **1005**, A9 (2025).

[39] T. Yasuda, I. Tanno, T. Hashimoto, K. Morinishi, and N. Satofuka, Artificial compressibility method using bulk viscosity term for an unsteady incompressible flow simulation, Comput. Fluids **258**, 105885 (2023).

[40] R. Temam, Une méthode d'approximation de la solution des équations de Navier-Stokes, Bul. Soc. Math. France **79**, 115 (1951).

[41] Y. Peng, W. Liao, L.-S. Luo, and L.-P. Wang, Comparison of the lattice Boltzmann and pseudo-spectral methods for decaying turbulence: Low-order statistics, Comput. Fluids **39**, 568 (2010).

[42] M. J. Lighthill, On sound generated aerodynamically I. General theory, Proc. R. Soc. A **211**, 564 (1952).

[43] Y. Qi, J. Shen, L.-P. Wang, and Z. Guo, Lifting relations for a generalized total-energy double-distribution-function kinetic model and their impact on compressible turbulence simulation, Comput. Fluids **280**, 106368 (2024).

[44] Y. Qi, L.-P. Wang, Z. Guo, and S. Chen, Consistent lifting relations for the initialization of total-energy double-distribution-function kinetic models, Phys. Rev. E **108**, 065301 (2023).

[45] A. H. Stroud, *Approximate Calculation of Multiple Integrals* (Prentice-Hall, Englewood Cliffs, NJ, 1971).

[46] L.-P. Wang, S. Chen, J. G. Brasseur, and J. C. Wyngaard, Examination of hypotheses in the Kolmogorov refined turbulence theory through high-resolution simulations. Part 1. Velocity field, J. Fluid Mech. **309**, 113 (1996).

[47] H. Helmholtz, LXIII. On integrals of the hydrodynamical equations, which express vortex-motion, London, Edinburgh, Dublin Philos. Mag. J. Sci. **33**, 485 (1867).

[48] J.-Z. Wu, H.-Y. Ma, and M.-D. Zhou, *Vortical Flows*, 1st ed. (Springer, New York, 2015).

[49] S. B. Pope, *Turbulent Flows* (Cambridge University, New York, 2000).

[50] T. Krüger, F. Varnik, and D. Raabe, Second-order convergence of the deviatoric stress tensor in the standard Bhatnagar-Gross-Krook lattice Boltzmann method, Phys. Rev. E **82**, 025701 (2010).

[51] Z. Guo and K. Xu, Progress of discrete unified gas-kinetic scheme for multiscale flows, Adv. Aerodyn. **3**, 6 (2021).

[52] L. Fu, X. Y. Hu, and N. A. Adams, A family of high-order targeted ENO schemes for compressible-fluid simulations, J. Comput. Phys. **305**, 333 (2016).

[53] U. Ghia, K. N. Ghia, and C. T. Shin, High-Re solutions for incompressible flow using the Navier-Stokes equations and a multigrid method, J. Comput. Phys. **48**, 387 (1982).